LAPPEENRANTA UNIVERSITY OF TECHNOLOGY

LUT School of Energy Systems

Degree Program in Electrical Engineering

Jouni Vuojolainen

ACTIVE MAGNETIC BEARING SYSTEM IDENTIFICATION METHODS AND ROTOR MODEL UPDATING

Examiners: Professor Olli Pyrhönen

D.Sc. Rafal Jastrzebski

ABSTRACT

Lappeenranta University of Technology

LUT School of Energy Systems

Degree Program in Electrical Engineering

Jouni Vuojolainen

Active Magnetic Bearing System Identification Methods and Rotor Model Updating

Master's Thesis

2.12.2015

74 pages, 22 figures, 9 tables, 1 appendix

Examiners: Professor Olli Pyrhönen

D.Sc. Rafal Jastrzebski

Supervisor: D.Sc. Alexander Smirnov

Keywords: active magnetic bearing, magnetic center, rotor model updating, stepped sine excitation, system identification

Active magnetic bearing is a type of bearing which uses magnetic field to levitate the rotor. These bearings require continuous control of the currents in electromagnets and data from position of the rotor and the measured current from electromagnets. Because of this different identification methods can be implemented with no additional hardware.

In this thesis the focus was to implement and test identification methods for active magnetic bearing system and to update the rotor model. Magnetic center calibration is a method used to locate the magnetic center of the rotor. Rotor model identification is an identification method used to identify the rotor model. Rotor model update is a method used to update the rotor model based on identification data. These methods were implemented and tested with a real machine where rotor was levitated with active magnetic bearings and the functionality of the methods was ensured. Methods were developed with further extension in mind and also with the possibility to apply them for different machines with ease.

TIIVISTELMÄ

Lappeenrannan Teknillinen Yliopisto

LUT School of Energy Systems

Sähkötekniikan koulutusohjelma

Jouni Vuojolainen

Aktiivisen magneettilaakerijärjestelmän identifiointimenetelmät ja roottorin mallin päivittäminen

Diplomityö

2.12.2015

74 sivua, 22 kuvaa, 9 taulukkoa, 1 liite

Tarkastajat: Professori Olli Pyrhönen

TkT Rafal Jastrzebski

Työn ohjaaja: TkT Alexander Smirnov

Hakusanat: aktiivinen magneettilaakeri, magneettinen keskipiste, roottorin mallin päivittäminen, porrastettu sini heräte, systeemin identifiointi

Aktiivinen magneettilaakeri on laakerityyppi, jossa magneettikenttä leijuttaa roottoria. Nämä laakerit vaativat jatkuvaa sähkömagneettien virransäätöä ja tietoa roottorin paikasta ja mitattuja virtoja sähkömagneeteista. Tämän takia erilaisia identifiointimenetelmiä voidaan toteuttaa pelkästään magneettilaakeria hyödyntäen.

Tässä työssä painopisteenä oli implementoida ja testata erilaisia identifiointimenetelmiä aktiiviseen magneettilaakerijärjestelmään ja päivittää roottorin mallia. Magneettisen keskipisteen kalibrointi on menetelmä, jolla roottorin magneettinen keskipiste etsitään. Roottorin mallin identifiointi on identifiointimenetelmä, jolla identifioidaan roottorin malli. Roottorin mallin päivittäminen on menetelmä, jolla roottorin mallia päivitetään identifioinnin perusteella. Nämä menetelmät toteutettiin ja testattiin oikealla moottorilla, jossa roottoria leijutettiin aktiivisilla magneettilaakereilla ja menetelmien toimivuus varmistettiin. Menetelmät suunniteltiin mahdolliset jatkokehitysmahdollisuudet huomioon ottaen ja lisäksi suunnittelussa otettiin huomioon erilaisten moottorien käyttäminen mahdollisimman vaivattomasti.

ACKNOWLEDGEMENTS

First of all, I'd like to thank Professor Olli Pyrhönen for giving me the opportunity to work with Master's thesis related to active magnetic bearings. Also his guidance and comments really helped me to finish this thesis before the end of year 2015.

Also thanks for D.Sc. Rafal Jastrzebski for having time to be the second examiner and commenting the thesis. Big thanks to the supervisor of the thesis D.Sc. Alexander Smirnov for commenting the thesis and help with the simulation models of the AMBs and with the rotor model updating also.

Lastly thanks to everyone else who in some way have helped me during the research and writing of the thesis.

Jouni Vuojolainen

Lappeenranta University of Technology

25.11.2015 Lappeenranta

CONTENTS

NOMENCLATURE

Symbols

a_j	polynomial coefficient of denominator
A	sine wave amplitude
A_{g}	stator pole face area
A_{min}	minimum sine wave amplitude value in identification
A_{max}	maximum sine wave amplitude value in identification
$A(\mathrm{j}f_k, \theta)$	identifiable transfer function denominator
b	equivalent iron flux path length
b_j	polynomial coefficient of numerator
b_{x}, b_{y}	error function dimension selection
$B(\boldsymbol{e})$	black box function, error function
$B(\mathrm{j}f_k, \theta)$	identifiable transfer function numerator
β_{x}	rotation around *x*-axis
β_{y}	rotation around *y*-axis
$\boldsymbol{C}(s)$	controller transfer function
$d_{ij,k}^{\mathrm{a,E}}$	anti-resonance damping ratio error

$d_{ij,k}^{\mathrm{r,E}}$	resonance damping ratio error
$\boldsymbol{D}$	damping matrix
e_p	design variable, elasticity value of the p:th element
$\boldsymbol{e}$	design variable vector used in the rotor model update
err_d	damping ratio error function
err_{f}	frequency error function
err_{tot}	total error function
$E(\mathrm{j}f_k)$	error between identifiable transfer function and identification data
$E^{\mathrm{LS}}(\mathrm{j}f_k)$	error in least squares approach
$\boldsymbol{E}$	excitation at controller input
$\boldsymbol{E}_{\mathrm{u}}$	excitation at controller output
f	sine wave frequency
f_k	frequency in hertz at k:th index
f_{x}	force acting on *x*-direction
f_{y}	force acting on *y*-direction
$f_{ij,k}^{\mathrm{a,E}}$	anti-resonance frequency error
$f_{ij,k}^{\mathrm{r,E}}$	resonance frequency error
F	force
$\boldsymbol{F}$	force vector
g_0	nominal airgap
g_{lower}	airgap in lower coil

g_{upper}	airgap in upper coil
$G(s)$	general transfer function
$G_{\mathrm{ETFE}}(f_{\mathrm{k}})$	empirical transfer function estimation function
$\hat{G}(\mathrm{j}f_k, \theta)$	identifiable transfer function
$G(\mathrm{j}f_k)$	frequency response function from identification data
$\boldsymbol{G}$	gyroscopic matrix
i	index of the FEM-model element
i,j	subscripts for excitation input and output axis
i_{b}	bias current
i_{c}	control current
i_{lower}	current in lower coil
i_{upper}	current in upper coil
I_{x}	transversal moment of inertia of x-axis
I_{y}	transversal moment of inertia of y-axis
I_{z}	rotational moment of inertia about the z-axis
$\boldsymbol{i}_{\mathrm{c}}$	control current vector
$\boldsymbol{I}$	identity matrix
j	imaginary unit
$\boldsymbol{J}$	Jacobian matrix
k	proportional constant
k	frequency index
k	resonance/anti-resonance peak index

$\boldsymbol{K}$	stiffness matrix
$\boldsymbol{K_i}$	current stiffness matrix
$\boldsymbol{K}_{\mathrm{x}}$	position stiffness matrix
$l_{\mathrm{LS}}(\theta)$	weighted linear least-squares cost function
L_{i}	flux path length in iron
μ_0	magnetic permeability of air
μ_{r}	relative magnetic permeability of rotor and stator material
m	mass of the rotor
m_{f}	number of flexible modes
$\boldsymbol{M}$	mass matrix
n	number of design values
n	order of the transfer function
n_{f}	number of total frequencies in parametric modeling
N	number of turns in the coil
$\boldsymbol{N}$	shape function matrix
$\widehat{\omega}^{\mathrm{r}}_{ij,k}$	resonance frequency from experimental data
$\widetilde{\omega}^{\mathrm{r}}_{ij,k}$	resonance frequency from model
$\widehat{\omega}^{\mathrm{a}}_{ij,k}$	anti-resonance frequency from experimental data
$\widetilde{\omega}^{\mathrm{a}}_{ij,k}$	anti-resonance frequency from model
Ω	rotational speed
$\boldsymbol{P}(s)$	controller transfer function
$\boldsymbol{\Phi}^{\mathrm{m}}$	reduced mode shape function matrix

$\boldsymbol{q}$	displacement vector
r	excitation signal
$r_{\min}$	minimum value of acceptable response in identification
$r_{\max}$	maximum value of acceptable response in identification
s	Laplace variable
s	longitudinal coordinate
$\boldsymbol{S}_{\mathrm{a}}$	actuator position transformation matrix
θ	angle between control and pole axis
θ_{x}	moment acting on *x*-direction
θ_{y}	moment acting on *y*-direction
$\boldsymbol{\theta}$	vector containing transfer function coefficients
$\boldsymbol{\theta}_a$	vector containing denominator coefficients
$\boldsymbol{\theta}_b$	vector containing numerator coefficients
$U(k)$	transfer function input
$\boldsymbol{U}_1$	controller output
$\boldsymbol{U}_2$	plant input
$\boldsymbol{V}_1$	controller input
$\mathbf{V}_2$	plant output
w_{d}	total error damping ratio weight
$w_{\mathrm{d},k}^{\mathrm{a}}$	anti-resonance damping ratio weight
$w_{\mathrm{d},k}^{\mathrm{r}}$	resonance damping ratio weight
$w_{\mathrm{f},k}^{\mathrm{a}}$	anti-resonance frequency weight

$w_{\mathrm{f},k}^{\mathrm{r}}$	resonance frequency weight
$W(\mathrm{j}f_k)$	weighting function in least squares approach
x	position of the rotor along the control axis
$x_{\mathrm{c},n}$	calculated rotor position at n:th iteration
$x_{\mathrm{s},n}$	rotor position set point at n:th iteration
$x_{\mathrm{s},n+1}$	rotor position set point for next iteration
$Y(k)$	transfer function output
$\hat{\zeta}_{ij,k}^{\mathrm{r}}$	damping ratio from experimental resonance frequency
$\tilde{\zeta}_{ij,k}^{\mathrm{r}}$	damping ratio from model anti-resonance frequency
$\hat{\zeta}_{ij,k}^{\mathrm{a}}$	damping ratio from experimental anti-resonance frequency
$\tilde{\zeta}_{ij,k}^{\mathrm{a}}$	damping ratio from model anti-resonance frequency

Abbreviations

AMB	active magnetic bearing
DOF	degree of freedom
DX	drive end *x*-axis
DY	drive end *y*-axis
ETFE	empirical transfer function estimate
FEM	finite element method
FRF	frequency response function
MIMO	multiple-input multiple-output
MPM	multi-point method
NX	non-drive end *x*-axis
NY	non-drive end *y*-axis
PLC	programmable logic controller
Z	axial *z*-axis

1 INTRODUCTION

Bearing is an element which constrains the relative motion to the desired motion only. Bearings also reduce the friction between these moving parts. Bearings are used in many applications, for example with electrical motors to allow only the axial rotation of the shaft. Different bearing types exist, one of the most common and well known is the ball bearing. Active Magnetic Bearing (AMB) is a type of bearing that uses magnetic levitation to support and carry the load. Load in this case is the rotor.

1.1 Active magnetic bearings

As mentioned, AMB is a bearing type which uses magnetic levitation to support the rotor. Easiest way would be to use permanent magnets to support the rotor, but it is not possible because Earnshaw's theorem says that a stable levitation cannot be achieved with fixed permanent magnets alone. Earnshaw's theorem however has exceptions or rather conditions that violate its assumptions, diamagnetic materials and feedback control with electromagnets can be used to achieve stable levitation (Gibbs, 1997). In case of AMBs electromagnets with feedback control are used to achieve the stable levitation.

In one axis case one electromagnet, power amplifier and feedback controller is used to levitate the rotor. Figure 1.1 shows an example of this case.

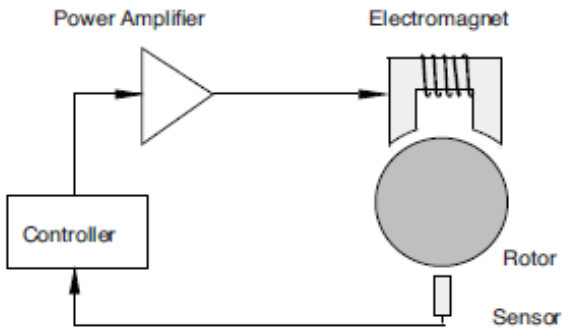

Fig. 1.1. Example of magnetic levitation in one axis case (Schweitzer, 2010).

In order to keep the rotor shown in Fig. 1.1 in stable position, current in the electromagnet's coil is altered with the controller. If rotor is too close to the electromagnet, current in the coil is decreased and vice versa. Real rotor however needs more electromagnets and in one axis two electromagnets are used in the opposite sides of the rotor. These electromagnets are then driven differentially. In the differential driving mode, bias current i_b and control current i_c are used to obtain the upper and lower coil current. Upper coil current is obtained by summing the control current i_c with the bias current i_b. Lower coil current is obtained with subtracting the control current from the bias current. These are expressed as

$$i_\mathrm{upper} = i_\mathrm{b} + i_\mathrm{c} \text{ and} \tag{1.1}$$

$$i_\mathrm{lower} = i_\mathrm{b} - i_\mathrm{c}. \tag{1.2}$$

Figure 1.2 shows the differential driving mode of the bearings.

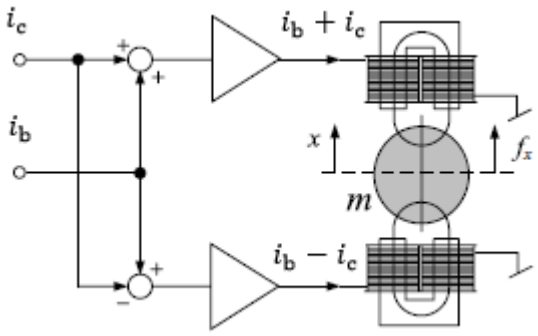

Fig. 1.2. Differential driving mode of the active magnetic bearing (Adapted from Schweitzer, 2010).

Typical rotor has two radial and one axial active magnetic bearing. One radial bearing consist of *x*- and *y*-axis so two differential driving bearings and four electromagnets are needed. Axial bearing is considered the *z*-axis and has one differential driving bearing. This AMB system is considered as a five degree of freedom (DOF) system. In total ten electromagnets are typically used.

Active magnetic bearings offer some advantages over other type of bearings (Schweitzer, 2010)

- Free of contact operation, absence of lubrication and contaminating wear. AMBs can be used in clean and sterile rooms, in vacuum systems and high temperatures also.
- Low bearing losses which are at high speeds five to 20 times less than journal or ball bearings.
- Rotors can be rotated at high speed. This speed is only limited by the strength of the rotor material.
- Because AMBs already need information from the system for control purposes, diagnostics are readily performed.
- Unbalance compensation of the rotor and force-free rotation is possible.
- Low maintenance costs and higher life time expectations due to lack of mechanical wear.
- Accurate position control, reference position tracking and vibration suppression are possible for some working conditions.

Disadvantages include

- Safety bearings needed in case of malfunction or overload, also rotor rests at the safety bearing when not in operation (Schweitzer, 2010).
- AMBs need electricity. In case of a power failure some consideration is needed if the rotor should be allowed to drop to the safety bearings or is some kind of uninterrupted power supply needed.
- Designing an AMB requires knowledge from mechatronics so in many fields of science, for example mechanical and electrical engineering (Schweitzer, 2010).
- Typically, the investments costs might be high (Schweitzer, 2010).
- The position sensors and controllers might require tuning, identification and recalibration at the end customer site. The controller might need updating whenever working condition change or when the machine/rotor is re-assembled.

1.2 Problem definition and hypothesis - Model based control and uncertainties

Model based control is a technique where controller is synthesized based on plant dynamics. This allows building more robust and better performance controllers, but these controllers tend to have a high order. (Smirnov, 2012)

However, a perfect model doesn't exist. This creates uncertainties to the model based control. In case of AMBs typical uncertainties are

- Variation in the manufacturing process (Smirnov, 2012). There is a limited accuracy which can be used to make for example the rotor, so the geometry of the rotor model is not fully the same as the manufactured rotor. Geometry changes might alter for example the readings of the position sensors. Position of the rotor and geometry of the rotor is thus uncertain and this decreases the controller performance.
- Sensor models are sometimes not included in the overall model of the system, because the cut-off frequency of the sensors might be very high (>10 kHz) or are modeled with just a simple first-order low-pass filter (Hynynen, 2011). In reality sensors might have a varying gain based on frequency and some noise is always present. Based on the level of the noise controller output has also some noise. Varying gain alters the sensor reading and the position of the rotor is in this case also uncertain and this decreases the controller performance.
- In AMB systems non-linearity of the AMB magnetic force for example is linearized in an operational point (Hynynen, 2011). Linearization assumes that some parameters are fixed, although they can change (Smirnov, 2012). If the AMB system is operated far from the operational point, control performance is decreased because linearization becomes less accurate.

In this thesis the research problem is to find ways to reduce the uncertainty related to the model based control. Methods are presented to reduce the uncertainty of the model based control.

1.3 Scope of work and outline

In this thesis the focus is on the AMB system identification methods and the rotor model update method. Implementation, design and testing of these methods is the main focus. All methods were also tested with a real machine where rotor was levitated with AMBs.

Chapter 1 provides the background and introduction to AMBs. Also model based control and uncertainties related to model based control are shown. Scope of work and motivation are presented.

In Chapter 2 rotor dynamics are presented. Rigid- and flexible rotor models are shown.

Chapter 3 presents the magnetic center calibration of the rotor. This is an identification method used to locate the magnetic center of the rotor. Magnetic center is an interesting point, because in that point force model of the bearing is satisfied for zero position offsets for all control axes (Prins, 2007). In the magnetic center the AMB system also corresponds better to the linearized equations and the uncertainty related to the model based control can be reduced. An algorithm using several bias current values for determining the magnetic center is presented. Contribution to the magnetic center calibration of the rotor was the developing, describing and testing of the algorithm using several bias current values based on method presented in (Prins, 2007).

In Chapter 4 identification of the rotor model is presented. Identification of the rotor model is a method used to obtain frequency response of the rotor-bearing system and to measure for example resonance and anti-resonance frequencies from the frequency response. An identification algorithm using step-sine signals and adaptive amplitude is presented. Based on the identification data a model of the system can be updated and tuned. Contribution to the rotor model identification was describing and extending the adaptive amplitude step-sine

identification algorithm and creating a way to save identification data to a file in real time for the specific platform.

Chapter 5 shows a method to update the rotor model. Rotor model update is a method used to obtain a model which more accurately describes the experimental data obtained with rotor model identification. A method for constructing the parametric model of the rotor from experimental data is presented. From this parametric model resonance and anti-resonance frequencies and damping ratios are extracted. Then a procedure is presented to obtain a more accurate rotor model based on experimental data. This updated rotor model could then be used to synthesize a new model based controller. Contribution to the rotor model update method was developing, describing, testing and extending the rotor model update method based on method presented in (Wróblewski, 2011).

Chapter 6 contains the test results from the magnetic center calibration presented in Chapter 3, identification of the rotor model presented in Chapter 4 and also from the rotor model update presented in Chapter 5. HS-Eden machine was used as the test machine.

Chapter 7 concludes the thesis. Future work suggestions are presented.

2 DYNAMICS OF THE ROTOR

In this chapter rigid and flexible rotor models are presented. Modeling of these rotors is done using linearized general equation of motion based on Newton's II law (Hynynen, 2011)

$$\boldsymbol{M}\ddot{\boldsymbol{q}}(t) + (\boldsymbol{D} + \Omega\boldsymbol{G})\dot{\boldsymbol{q}}(t) + \boldsymbol{K}\boldsymbol{q}(t) = \boldsymbol{F}(t), \tag{2.1}$$

where $\boldsymbol{M}$ is the mass matrix, $\boldsymbol{D}$ is the damping matrix, Ω is the rotational speed**,** $\boldsymbol{G}$ is the gyroscopic matrix, $\boldsymbol{K}$ is the stiffness matrix, $\boldsymbol{q}$ is the displacement vector and $\boldsymbol{F}$ is a force vector. This linearization can be used if assuming that the rotor is axisymmetric, displacements from reference points are small compared to the rotor dimensions and that the rotational speed is constant (Hynynen, 2011).

2.1 Rigid rotor model

Assumption about rigid rotor model is true when rotor has all the flexible eigenfrequencies above the bandwidth of the position sensor and the maximum rotational speed (Hynynen, 2011). Assuming a rigid rotor with two radial magnetic bearings, Equation (2.1) describes the motion of the rotor with respect to the center of the mass with state vector $\boldsymbol{q} = [x \quad y \quad \beta_{\mathrm{x}} \quad \beta_{\mathrm{y}}]^{\boldsymbol{T}}$. Displacement along particular axis is denoted with *x* and *y*, β_{x} and β_{y} are the rotations around the *x*- and *y*-axes respectively. This system is presented as four degrees of freedom system. Motion along the *z*-axis, which is the fifth DOF, is not coupled with the other DOFs and it is treated separately with the axial magnetic bearing. Rotation around the *z*-axis is the sixth degree of freedom and it is included indirectly in the gyroscopic matrix as a multiplier. (Smirnov, 2012) For the undamped rigid body the Eq. (2.1) is formulated as (Adapted from Smirnov, 2012)

$$\boldsymbol{M}\ddot{\boldsymbol{q}} + \Omega\boldsymbol{G}\dot{\boldsymbol{q}} = \boldsymbol{F}. \tag{2.2}$$

Matrices from Eq. (2.2) are constructed as (Adapted from Smirnov, 2012)

$$\boldsymbol{M} = \begin{bmatrix} m & 0 & 0 & 0 \\ 0 & m & 0 & 0 \\ 0 & 0 & I_{\mathrm{x}} & 0 \\ 0 & 0 & 0 & I_{\mathrm{y}} \end{bmatrix}, \tag{2.3}$$

$$\boldsymbol{G} = \begin{bmatrix} 0 & 0 & 0 & 0 \\ 0 & 0 & 0 & 0 \\ 0 & 0 & 0 & I_{\mathrm{z}} \\ 0 & 0 & -I_{\mathrm{z}} & 0 \end{bmatrix} \text{ and} \tag{2.4}$$

$$\boldsymbol{F} = \begin{bmatrix} f_{\mathrm{x}} \\ f_{\mathrm{y}} \\ \theta_{\mathrm{x}} \\ \theta_{\mathrm{y}} \end{bmatrix}, \tag{2.5}$$

where m is the mass of the rigid rotor, I_{x} is the transversal moment of inertia of x-axis, I_{y} is the transversal moment of inertia of y-axis, I_{z} is the rotational moment of inertia about the z-axis, f_{x} is the force acting on x-direction, f_{y} is the force acting on y-direction, θ_{x} and θ_{y} are the moments applied to the same axis. Figure 2.1 demonstrates these coordinates.

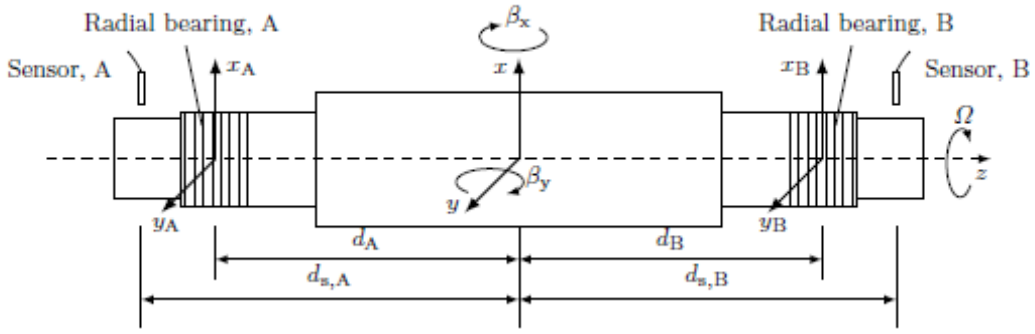

Fig. 2.1. Demonstration of the rotor coordinate systems (Smirnov, 2012).

With AMB systems it is conventional to reformulate Eq. (2.2) which relates to the center of the mass to relate to the bearing coordinates (Smirnov, 2012)

$$\boldsymbol{M}_{\mathrm{b}}\ddot{\boldsymbol{q}}_{\mathrm{b}} + \Omega\boldsymbol{G}_{\mathrm{b}}\dot{\boldsymbol{q}}_{\mathrm{b}} = \boldsymbol{K}_{\mathrm{x}}\boldsymbol{q}_{\mathrm{b}} + \boldsymbol{K}_{\mathrm{i}}\boldsymbol{i}_{\mathrm{c}}, \tag{2.6}$$

where subscript b denotes the bearing coordinates $\boldsymbol{q}_{\mathrm{b}} = [x_A \quad y_{\mathrm{A}} \quad x_{\mathrm{B}} \quad y_{\mathrm{B}}]$, x_{A} and x_{B} denote the displacement along *x*-axis and y_{A} and y_{B} denote the displacement along y-axis, $\boldsymbol{K}_{\mathrm{x}}$ is the position stiffness matrix, $\boldsymbol{K}_{\mathrm{i}}$ is the current stiffness matrix and control current vector $\boldsymbol{i}_{\mathrm{c}} = [i_{\mathrm{c,x,A}} \quad i_{\mathrm{c,y,A}} \quad i_{\mathrm{c,x,B}} \quad i_{\mathrm{c,y,B}}]$ denotes the current in *x*- and *y*-directions of electromagnets at magnetic bearings A and B. Transformation from center coordinates to bearing coordinates is shown in (Smirnov, 2012) and (Hynynen, 2011).

2.2 Flexible rotor model

Flexible rotor is a type of rotor that has flexible eiqenfrequencies at low frequencies also and they can be affected with position controller (Hynynen, 2011). Flexible rotors require the modeling of the elasticity behavior of materials (Lösch, 2002). In reality pure rigid rotor shown in Ch. 2.1 does not exist.

Flexible rotors are modeled with Finite Element Method (FEM) modeling by dividing the rotor into a finite set of similar elements. Elements of the rotor are presented by cylinders, because rotors are usually axisymmetric in the *xy*-plane. These cylinders behavior is described by Timoshenko beam theory. Timoshenko beam elements take into account the rotational inertia of the rotor and shear deformation, which is useful for short and very thick rotors. (Smirnov, 2012) Figure 2.2 shows an example of one beam element.

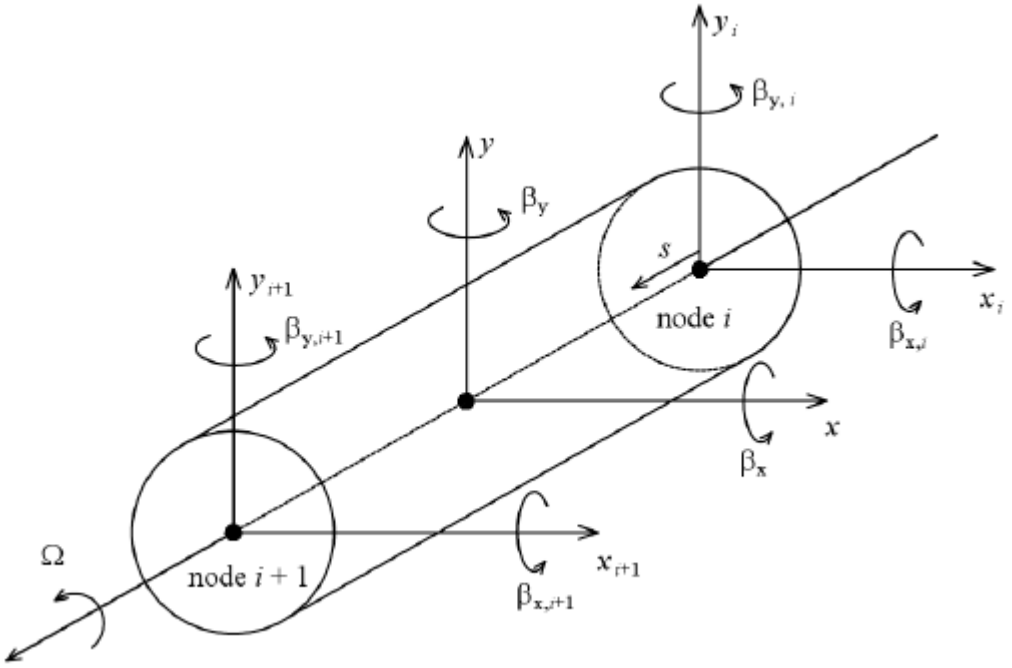

Fig. 2.2. One beam element of the FEM-model (Hynynen, 2011).

Equation of motion presented in Eq. (2.1) is used to describe each beam element of the FEM-model (Smirnov, 2012)

$$\boldsymbol{M}_i\ddot{\boldsymbol{q}}_i + (\boldsymbol{D}_i + \Omega\boldsymbol{G}_i)\dot{\boldsymbol{q}}_i + \boldsymbol{K}_i\boldsymbol{q}_i = \boldsymbol{F}_i, \tag{2.7}$$

where matrices corresponds to the Eq. (2.1) but now for the i:th beam element. State vector $\boldsymbol{q}_i$ is $\boldsymbol{q}_i = [x_i \quad y_i \quad \beta_{\mathrm{x},i} \quad \beta_{\mathrm{y},i}]^{\boldsymbol{T}}$.

Shape function matrix $\boldsymbol{N}$ is then used to describe the final shape of rotor (Smirnov, 2012)

$$\boldsymbol{q}_i^{\mathrm{g}} = \boldsymbol{N}(s)\boldsymbol{q}_i, \tag{2.8}$$

where s is the longitudinal coordinate for each node and superscript g describes the global coordinate system. Equation of motion (2.1) is then used in global coordinate system (Smirnov, 2012)

$$\boldsymbol{M}^{\mathrm{g}}\ddot{\boldsymbol{q}}^{\mathrm{g}} + (\boldsymbol{D}^{\mathrm{g}} + \Omega\boldsymbol{G}^{\mathrm{g}})\dot{\boldsymbol{q}}^{\mathrm{g}} + \boldsymbol{K}^{\mathrm{g}}\boldsymbol{q}^{\mathrm{g}} = \boldsymbol{F}^{\mathrm{g}}, \tag{2.9}$$

where state vector $\boldsymbol{q}^{\mathrm{g}} = \begin{bmatrix} \boldsymbol{q}_1^{\mathrm{g}} & \boldsymbol{q}_2^{\mathrm{g}} & \cdots & \boldsymbol{q}_P^{\mathrm{g}} \end{bmatrix}$ is the global displacement vector. Usually Eq. (2.9) is not used because it has a great number of state-variables and modal reduction techniques are used to include the required information only (Smirnov, 2012). After modal reduction and adding the linearized forces provided by electromagnets to the equation of motion of the flexible rotor, overall plant model of the system is (Smirnov, 2012)

$$\boldsymbol{M}^{\mathrm{m}}\ddot{\boldsymbol{q}}^{\mathrm{m}} + (\boldsymbol{D}^{\mathrm{m}} + \Omega\boldsymbol{G}^{\mathrm{m}})\dot{\boldsymbol{q}}^{\mathrm{m}} + (\boldsymbol{K}^{\mathrm{m}} + \boldsymbol{K}_{\mathrm{x}}^{\mathrm{m}})\boldsymbol{q}^{\boldsymbol{m}} = \boldsymbol{K}_{\mathrm{i}}^{\mathrm{m}}\boldsymbol{i}_{\mathrm{c}}, \tag{2.10}$$

where negative position stiffness $\boldsymbol{K}_{\mathrm{x}}^{\mathrm{m}}$ and current stiffness $\boldsymbol{K}_{\mathrm{i}}^{\mathrm{m}}$ are expressed as (Smirnov, 2012)

$$\boldsymbol{K}_{\mathrm{x}}^{\mathrm{m}} = (\boldsymbol{\Phi}^{\mathrm{m}})^{\mathrm{T}}\boldsymbol{S}_{\mathrm{a}}(-\boldsymbol{K}_{\mathrm{x}})\boldsymbol{\Phi}^{\mathrm{m}} \text{ and} \tag{2.11}$$

$$\boldsymbol{K}_{\mathrm{i}}^{\mathrm{m}} = (\boldsymbol{\Phi}^{\mathrm{m}})^{\mathrm{T}}\boldsymbol{S}_{\mathrm{a}}\boldsymbol{K}_{\mathrm{i}}\boldsymbol{\Phi}^{\mathrm{m}}. \tag{2.12}$$

Position of the actuators are included in the matrix $\boldsymbol{S}_{\mathrm{a}}$ and $\boldsymbol{\Phi}^{\mathrm{m}}$ is the reduced mode shape function matrix in modal coordinates.

3 MAGNETIC CENTER CALIBRATION OF THE ROTOR

This chapter describes usage of AMBs as a force measurement tool. Multi-point method (MPM) and bias current perturbation method are presented. This information can be used to determine the magnetic center of the rotor, also known as radial origin and effective rotor origin. Algorithm for magnetic center calibration is presented. Also notes about implementation for Beckhoff programmable logic controller (PLC) system are shown.

3.1 AMB force measurement

In a standard AMB system force measurement by observing coil currents and air gaps is possible. In this thesis a common eight pole radial AMB with two control axes is studied. A pair of eight pole heteropolar AMBs comprises the full radial system. Control axes in this case are drive end *x*-axis (DX), drive end *y*-axis (DY), non-drive end *x*-axis (NX) and non-drive end *y*-axis (NY). Assuming no magnetic coupling between these control axes, force acting in one control axis is according to (Gähler, 1994a)

$$F = k\left[\frac{i_{\mathrm{upper}}^2}{(2g_{\mathrm{upper}})^2} - \frac{i_{\mathrm{lower}}^2}{(2g_{\mathrm{lower}})^2}\right], \tag{3.1}$$

where i_{upper} is the current in upper coil, i_{lower} is the current in lower coil, g_{upper} is airgap in the upper coil and g_{lower} is the airgap in lower coil. k is a proportional constant which is given by

$$k = \mu_0 A_{\mathrm{g}} N^2 \cos\theta, \tag{3.2}$$

where μ_0 is the magnetic permeability of air, A_{g} is the stator pole face area, N is the number of turns in the coil and θ is the angle between control and pole axis. This geometry is shown in Fig. 3.1.

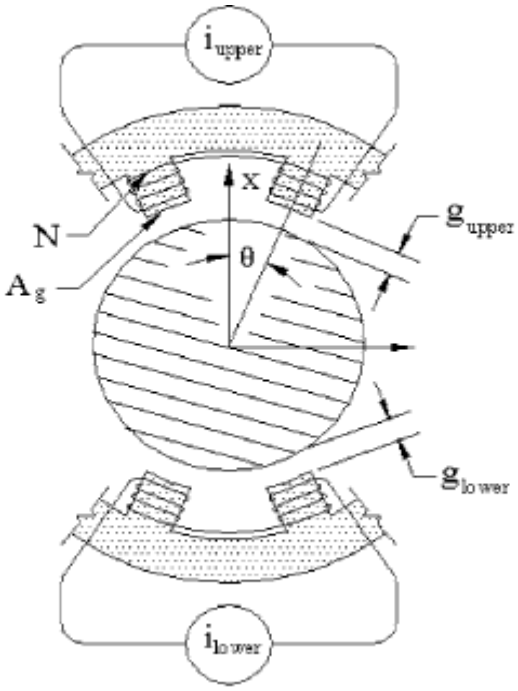

Fig. 3.1. Geometry of one control axis (Prins, 2007).

Airgaps g_{upper} and g_{lower} can be rewritten to relate to the rotor position along the control axis (Gähler, 1994a)

$$g_{\text{upper}} = g_0 - x\cos\theta \text{ and} \tag{3.3}$$

$$g_{\text{lower}} = g_0 + x\cos\theta, \tag{3.4}$$

where g_0 is the nominal airgap and x is the position of the rotor along the control axis. This form of airgaps is used in this thesis.

According to (Prins, 2007) Equation (3.1) is simplified as it neglects the flux path in the rotor and stator. This can be correlated by adding an equivalent iron flux path length b to the air gap length in Eq. (3.1). Equivalent iron flux path length can be expressed as

$$b = \frac{L_{\text{i}}}{\mu_{\text{r}}}, \tag{3.5}$$

where L_i is the flux path length in iron and μ_r is the relative magnetic permeability of rotor and stator material.

Now combining Eq. (3.1) and Eqs. (3.3)-(3.5) force measurement equation is written as (Prins, 2007)

$$F = k\left[\frac{i_{\text{upper}}^2}{(2(g_0 - x\cos\theta)+b)^2} - \frac{i_{\text{lower}}^2}{(2(g_0 + x\cos\theta)+b)^2}\right]. \quad (3.6)$$

This form of the force equation is used in this thesis.

3.2 Multi-point method and bias current perturbation method

Magnetic center of the rotor is a point where the force model of the bearing is satisfied for zero position offsets for all control axes (Prins, 2007). When operating in this point, the AMB system corresponds better to the linearized equations. In addition in this point the actuator usage is minimized and based on this power usage of AMBs is also minimized. Therefore leading to the system that is more efficient. In the magnetic center, the force availability is maximized in any direction (DX, DY, NX, NY).

Multi-point method (MPM) is a technique used to predict forces acting on the rotor and rotor position using information from coil currents only. This method is very useful for the field conditions and can be used on existing systems. MPM takes an advantage of the AMB system feedback to keep the rotor at a fixed position during operation. (Marshall, 2001)

MPM is used in a single control axis. Rotor position and forces are estimated by applying multiple current differences to either the lower or the upper coil. Assuming current increase in the upper coil, AMB system has to increase the current in the lower coil to compensate the extra force created. Now a pair of upper and lower coil currents is obtained. The process is

repeated with different current to obtain all the pairs. After several measurements rotor location x and supported force F can be determined. (Marshall, 2001)

Based on MPM (Prins, 2007) introduced a method called bias current perturbation method. This method is used to locate the magnetic center of the rotor. In this method, controller's ability to support the rotor at a specific position for any bias current value is used. This method is also used for a single control axis. When bias current value is changed, in order to keep the rotor at the same position, controller current pair values i_{upper} and i_{lower} change. Because rotor position and the force is not altered when changing bias current, these pairs of i_{upper} and i_{lower} values are considered to be simultaneous equations and can be used to determine the force F and rotor position x from Eq. (3.6).

Considering that we have two current pairs $(i_{\text{lower},1}, i_{\text{upper},1})$ and $(i_{\text{lower},2}, i_{\text{upper},2})$ resulting from two different bias currents. These current pairs are then used with Eq. (3.6) forming two separate expressions of Eq. (3.6). Value of *x* can then be solved with setting these expressions as equal

$$\frac{i_{\text{upper},2}^2}{(2(g_0-x\cos\theta)+b)^2}-\frac{i_{\text{lower},2}^2}{(2(g_0+x\cos\theta)+b)^2}=\frac{i_{\text{upper},1}^2}{(2(g_0-x\cos\theta)+b)^2}-\frac{i_{\text{lower},1}^2}{(2(g_0+x\cos\theta)+b)^2}. \tag{3.7}$$

Now solving for rotor position x in Eq. (3.7) results (Prins, 2007)

$$x=\frac{1}{\cos\theta}\left[\frac{2g_0+b}{i_{\text{lower},1}^2-i_{\text{lower},2}^2-i_{\text{upper},1}^2+i_{\text{upper},2}^2}\right]*\left[\frac{i_{\text{lower},1}^2-i_{\text{lower},2}^2+i_{\text{upper},1}^2-i_{\text{upper},2}^2}{2}\right]$$

$$\pm\sqrt{(i_{\text{lower},1}^2-i_{\text{lower},2}^2)(i_{\text{upper},1}^2+i_{\text{upper},2}^2)}. \tag{3.8}$$

Equation (3.7) is quadratic and has two roots, but the correct root is easily identified, because it is the only root *x* that exists in the physical boundaries of the stator. Rotor position value x is considered as an error/offset value for the position control and this value is used to guide the rotor to the magnetic center. This error is initially nonzero, so an iterative equation is presented for calculating the new position reference for the position controller (Prins, 2007)

$$x_{\mathrm{s},n+1} = x_{\mathrm{s},n} - x_{\mathrm{c},n}, \tag{3.9}$$

where $x_{\mathrm{s},n+1}$ is the position controller set point for the next iteration, $x_{\mathrm{s},n}$ is the current position controller set point and $x_{\mathrm{c},n}$ is the calculated rotor position from Eq. (3.8). Initial set point for the controller is zero. In ideal case iteration is continued until $x_{\mathrm{c},n}$ is zero, but in practice a reasonably small limit is defined. In most cases, it is based on the sensor noise. When iteration is finished and $x_{\mathrm{c},n}$ is between acceptable limits, for that control axis magnetic center is found.

It should be noted that at least three different bias current values should be used to remove possible outliers from current measurements (Prins, 2007). From these three bias current values three pairs of bias currents can be used ($I_{\mathrm{b1}}, I_{\mathrm{b2}}$), ($I_{\mathrm{b1}}, I_{\mathrm{b3}}$) and ($I_{\mathrm{b2}}, I_{\mathrm{b3}}$). Equation (3.8) can then be used for all these pairs and average value is used for calculating new position reference for the controller in Eq. (3.9).

3.3 Implementation of the algorithm with several bias current values

An algorithm was developed for the magnetic center calibration with a Simulink® model. Calibration is done for all of the control axes (DX, DY, NX, NY) at the same time. In this case iteration is continued until all control axes rotor position errors satisfy an acceptable limit. Coil currents i_{upper} and i_{lower} are measured from frequency converters which are driving the coils and are averaged over a one second sample.

This algorithm uses five different bias current values based on selected bias current i_{b}

1. i_{b} decreased by 20% (i_{b1})
2. i_{b} decreased by 10% (i_{b2})
3. i_{b} (i_{b3})
4. i_{b} increased by 10% (i_{b4})
5. i_{b} increased by 20% (i_{b5}).

From these five bias current values ten different bias current pairs are possible

1. i_{b1} and i_{b2}
2. i_{b1} and i_{b3}
3. i_{b1} and i_{b4}
4. i_{b1} and i_{b5}
5. i_{b2} and i_{b3}
6. i_{b2} and i_{b4}
7. i_{b2} and i_{b5}
8. i_{b3} and i_{b4}
9. i_{b3} and i_{b5}
10. i_{b4} and i_{b5}.

First, pair 1 is selected and then magnetic center is determined with bias current values i_{b1} and i_{b2}. Then pair 2 is selected and magnetic center is determined again based on bias current values i_{b1} and i_{b3}. After all pairs have been used an average is calculated and that location is assumed as the true magnetic center. Flowchart of the magnetic center calibration is shown in Figure 3.2.

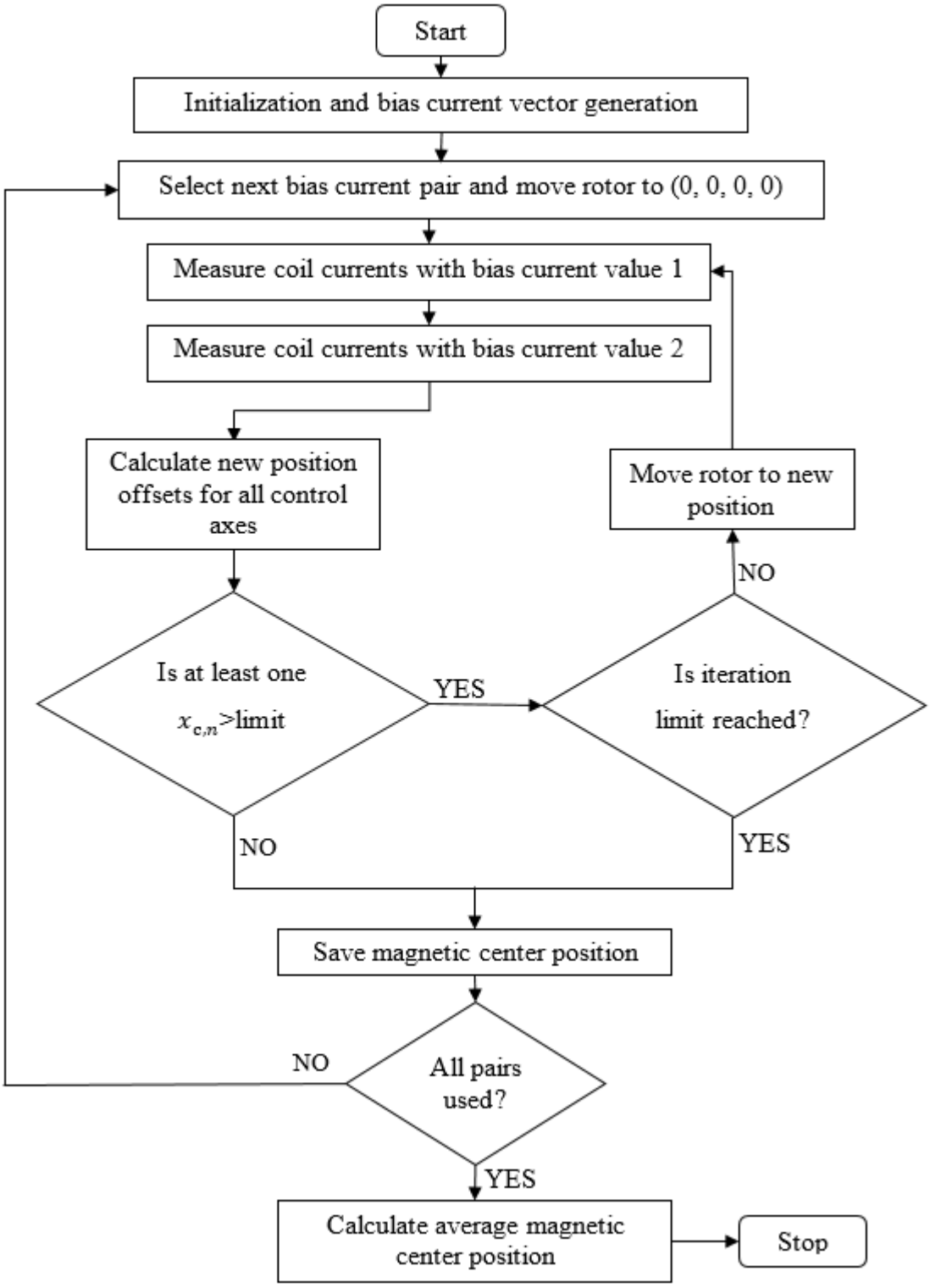

Fig. 3.2. Flowchart of the magnetic center calibration algorithm. $x_{c,n}$ is the offset/error of one control axis.

Parameters of the magnetic center calibration algorithm are tunable, so calibration with different AMB systems is possible with simple and fast modifications. Additionally, a warning is issued when iteration limit is reached.

3.4 Notes on implementation for the Beckhoff programmable logic controller system

Beckhoff is a German company providing PC-based PLC system automation software and hardware. Main software product is the TwinCAT platform, which is an automation and a real-time package for PCs. TwinCAT is basically an all-in-one software, where additional functionalities can be added as separate functions as needed. In TwinCAT different automation programming languages can be used for example C/C++, Structured text and Simulink®. Minimum cycle time that can be achieved with TwinCAT is 50 µs (Beckhoff 2012). Because Simulink® models in TwinCAT have a fixed cycle time, variable-step solver in Simulink® cannot be used. Also cycle time of each model should be adjusted so that the model doesn't exceed the desired cycle time (because of heavy calculations etc.), because this affects the other models in TwinCAT.

Beckhoff also provides a wide variety of hardware to use with TwinCAT, different input and output terminals for connecting a variety of fieldbus components and also for example custom PCs. EtherCAT is the standard communication protocol in the Beckhoff PLC systems, and it was developed by Beckhoff.

In this case control of the AMB system and magnetic center calibration is done in a TwinCAT project with the use of Simulink® models, which are then compiled to TwinCAT by using a specific TwinCAT target in the Simulink®. A custom PC from Beckhoff was used to run the TwinCAT project, model number of the custom PC was C6930-0050. This custom PC is made to fit inside control cabinet. Processor of the custom PC was Intel® Core™ i7-4700EQ @ 2.4 GHz and it had 16 GB of RAM. Operating system used was Microsoft® Windows® 7 Professional and TwinCAT version used was 3.1.4018.16.

4 ROTOR MODEL IDENTIFICATION

In this chapter system identification theory is presented and applied to AMB system in frequency domain. Identifiable transfer functions are described. An adaptive amplitude step-sine identification algorithm is presented. Additional notes about implementation for the Beckhoff PLC system are given.

4.1 AMB System Identification

System identification is used to build mathematical models of systems based on measured and observed data from systems. Usually this input-output data is recorded during a specific identification experiment. This is done to make the data maximally informative. (Ljung, 1987)

Different identification experiments exist. One type is step- and impulse response experiments. Also sine waves are used in identification experiments (Keesman, 2011). Sine wave identification experiments can be divided into two groups: stepped sine, which has all the power on one frequency and multisine, which has power divided to different frequencies.

After experiments a frequency response function (FRF) is formed. There are different estimation methods for frequency response functions. Comparison of these methods in AMB systems has been done in (Hynynen, 2010). In this case simplest FRF, empirical transfer function estimate (ETFE) is used

$$G_{\mathrm{ETFE}}(f_k) = \frac{Y(k)}{U(k)}, \tag{4.1}$$

where $Y(k)$ is the transfer function output and $U(k)$ is the transfer function input at f_k:th frequency. k is the frequency index.

Forces acting on rotor can be measured when the rotor is levitated with AMBs. Excitation is also possible with AMBs. (Gähler, 1998) Based on this, AMB system identification is possible

with no additional hardware. Sine wave excitation is typically used with AMB system identification. Identification is done in the frequency domain.

An ISO standard has emerged for signals and excitation locations used in AMB system frequency response measurements (ISO 14839-3, 2006). Figure 4.1 shows a general block diagram used with the ISO standard.

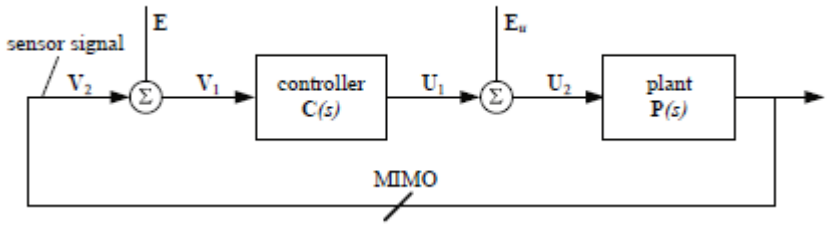

Fig. 4.1. Block diagram showing signals and excitation locations for frequency measurements according to the ISO standard (ISO 14839-3, 2006).

Figure 4.1 shows the possible inputs, outputs and excitations used for AMB system identification. The excitation signal $\boldsymbol{E}$ is located at controller input and the excitation $\boldsymbol{E}_{\mathrm{u}}$ is located at the controller output. $\boldsymbol{V}_1$ is the controller input and $\boldsymbol{U}_2$ is the plant input. $\mathbf{V}_2$ is the plant output and $\boldsymbol{U}_1$ is the controller output signal. Now based on inputs, outputs and excitation signals different transfer functions can be identified. Table 4.1 shows the different transfer functions, which can be identified.

Table 4.1. Transfer functions, which can be identified from frequency response measurement. Adapted from (Schweitzer, 2010).

transfer function type	excitation location	transfer function name	$\boldsymbol{G}(s)$	system properties validated
$\boldsymbol{U}_2 \rightarrow \boldsymbol{V}_2$	$\boldsymbol{E}_\mathrm{u}$	open-loop plant	$\boldsymbol{P}(s)$	identification of plant dynamics
$\boldsymbol{V}_1 \rightarrow \boldsymbol{U}_1$	$\boldsymbol{E}$	controller	$\boldsymbol{C}(s)$	controller performance
$\boldsymbol{E} \rightarrow \boldsymbol{V}_1$	$\boldsymbol{E}$	input sensitivity	$[\boldsymbol{I} - \boldsymbol{P}(s)\boldsymbol{C}(s)]^{-1}$	robustness to uncertainties
$\boldsymbol{E}_\mathrm{u} \rightarrow \boldsymbol{V}_2$	$\boldsymbol{E}_\mathrm{u}$	dynamic compliance	$[\boldsymbol{I} - \boldsymbol{P}(s)\boldsymbol{C}(s)]^{-1}\boldsymbol{P}(s)$	attenuation, resonances, transmission zeroes
$\boldsymbol{V}_2 \rightarrow \boldsymbol{E}_\mathrm{U}$	$\boldsymbol{E}_\mathrm{u}$	dynamic stiffness	$\boldsymbol{P}^{-1} - \boldsymbol{C}$	static and dynamic stiffness
$\boldsymbol{E}_\mathrm{u} \rightarrow \boldsymbol{U}_2$	$\boldsymbol{E}_\mathrm{u}$	output sensitivity	$[\boldsymbol{I} - \boldsymbol{C}(s)\boldsymbol{P}(s)]^{-1}$	identical to input sensitivity only in SISO case
$\boldsymbol{V}_1 \rightarrow \boldsymbol{V}_2$	$\boldsymbol{E}$	Nyquist, open-loop system	$\boldsymbol{P}(s)\boldsymbol{C}(s)$	Nyquist diagram

Now it should be noted that the plant (rotor) should be levitated during the identification procedure. This is especially important when identifying the open-loop plant $\boldsymbol{P}(s)$ to prevent the possible rotor-stator contact. According to (Schweitzer, 2010) it is possible to obtain open-loop measurement from closed-loop system.

This thesis focuses on the rotor model identification, so excitation at $\boldsymbol{E}_{\mathrm{u}}$ is used and plant input $\boldsymbol{U}_2$ and plant output $\boldsymbol{V}_2$ are measured to form the open-loop plant $\boldsymbol{P}(s)$. With $\boldsymbol{E}_{\mathrm{u}}$ excitation, also according to Table 4.1 dynamic compliance, dynamic stiffness and output sensitivity transfer functions are possible to identify.

4.2 Implementation of step sine identification algorithm with adaptive amplitude

An algorithm was developed for the rotor model identification. Identification algorithm was developed with a Simulink® model. Algorithm uses step sine waves and sine wave amplitude is adapted to get an acceptable response. This sine wave is used as the excitation $\boldsymbol{E}_{\mathrm{u}}$. Sine wave equation in time domain is

$$r = A\sin(2\pi f t), \tag{4.2}$$

where r is the excitation signal, A is the amplitude (in amperes) and f is the sine wave frequency. Amplitude A is changed until the maximum response value of V_2**,** for the axis where excitation is applied, is between $r_{\min}$ and $r_{\max}$. In this case $r_{\min}$ equals 20 µm and $r_{\max}$ equals 50 µm. If response is less than $r_{\min}$, amplitude is increased by 20%. If response is greater than $r_{\max}$, amplitude is decreased by 20%. When response is between $r_{\min}$ and $r_{\max}$, identification data is saved and next frequency is selected. Also if amplitude is less than $A_{\min}$ or greater than $A_{\max}$, identification data is saved and next frequency is selected. In this case $A_{\min}$ equals 50 mA and $A_{\max}$ equals 3 A.

Frequency range of the identification algorithm can be tuned to include and focus on specific frequencies. Frequency range is generated as linearly spaced points between selected starting and ending frequency.

Identification algorithm starts by exiting radial axes in order DX, DY, NX, NY one axis at a time. After all frequencies are exited for one radial axis, next radial axis is selected. Every radial axis plant input U_2 and plant output V_2 are measured so cross coupling of the radial axes can be investigated. In addition, the real currents from frequency converters are saved for the exited axis. After radial excitations, axial excitation (Z-axis) is performed as a separate experiment. Also the real currents from axial frequency converter are saved. Flowchart of the identification algorithm is shown in Figure 4.2.

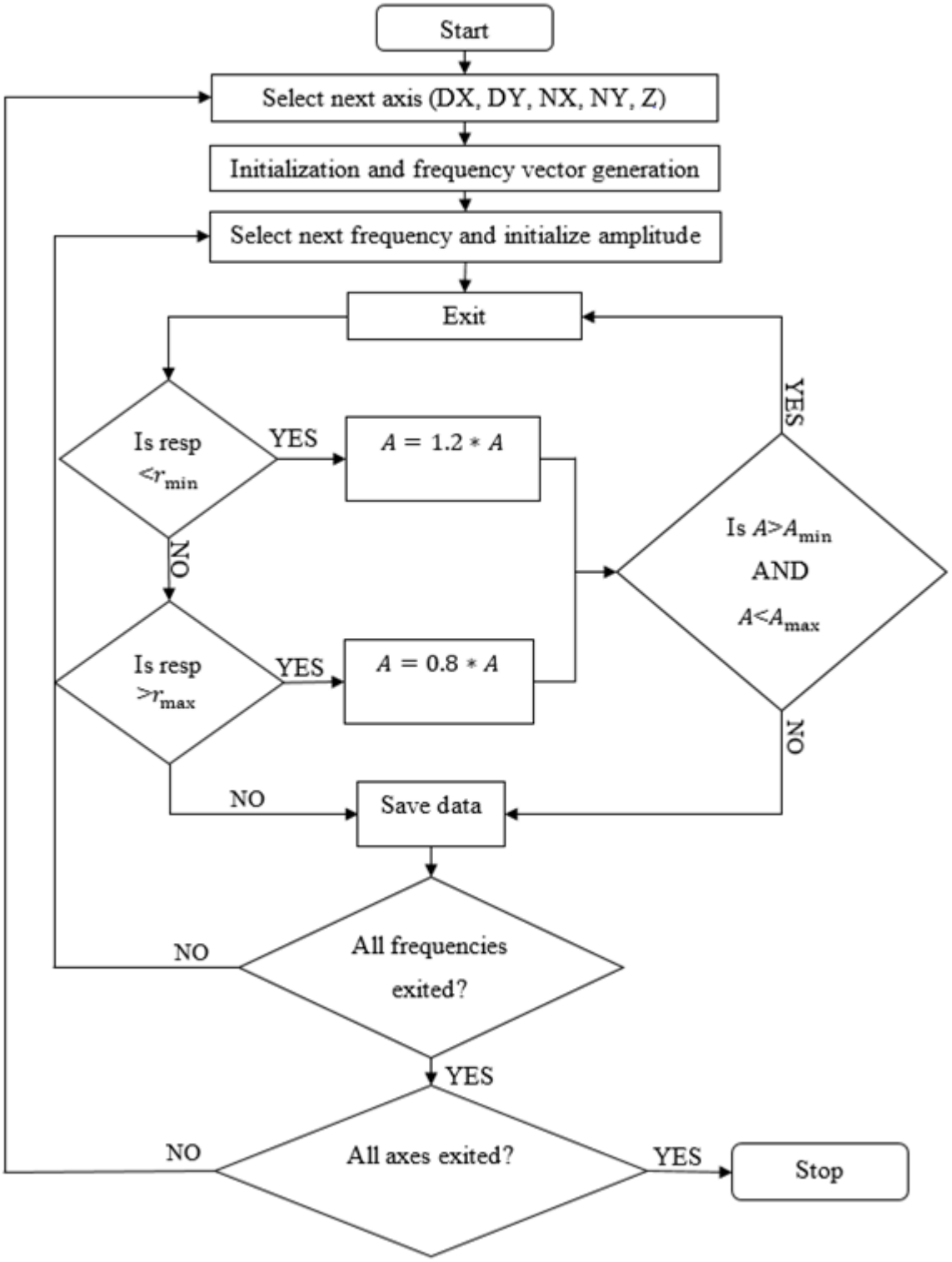

Fig. 4.2. Flowchart of the identification algorithm. Resp is the maximum response value of V_2 for the exited axis.

When identification has finished all data has been saved to an ".m" file. This file can be directly run in MATLAB® generating matrix form data of measurements. After loading the file post processing is possible with MATLAB®.

It should be noted that MATLAB® functions linspace and logspace cannot be used in the algorithm because output size of these functions is undefined. When compiling the algorithm to the Beckhoff TwinCAT all vectors/matrices must have fixed dimensions. Because of this own implementation of linspace-function has been used.

5 ROTOR MODEL UPDATE BASED ON IDENTIFICATION

This chapter describes a method for updating FEM-model of the rotor based on experimental identification data. Moreover, parametric modeling based on identification data is presented. This modeling is applied to locate poles and zeros of the open-loop plant transfer function presented in the identification data. A simple example is given to demonstrate the rotor model update method.

5.1 Parametric modeling and finding pole- and zero-frequencies

Identification data can be used to make a parametric model of the rotor. From this parametric model poles and zeros can be extracted. Parametric model identification has been discussed in (Verboven, 2002) and (Hynynen, 2011).

Identifiable parametric frequency response function at frequency f_k between transfer function input and output can be written as (Verboven, 2002)

$$\hat{G}(\mathrm{j}f_k, \theta) = \frac{B(\mathrm{j}f_k, \theta)}{A(\mathrm{j}f_k, \theta)}, \tag{5.1}$$

where $B(\mathrm{j}f_k, \theta)$ is the identifiable transfer function numerator and $A(\mathrm{j}f_k, \theta)$ is the identifiable transfer function denominator, θ is the parametric vector containing numerator or denominator polynomial coefficients and k is the frequency index. Numerator and denominator can be written as a sum of polynomial coefficients

$$B(\mathrm{j}f_k, \theta) = \sum_{j=0}^{n} b_j f_k^{\,j} \text{ and} \tag{5.2}$$

$$A(\mathrm{j}f_k, \theta) = \sum_{j=0}^{n} a_j f_k^{\,j}. \tag{5.3}$$

These polynomial coefficients b_j and a_j are estimated based on identification data. n is the order of the transfer function polynomial.

Parameters are estimated based on error between identifiable transfer function $\hat{G}(\mathrm{j}f_k, \theta)$ and FRF obtained from identification data $G(\mathrm{j}f_k)$

$$E(\mathrm{j}f_k) = \hat{G}(\mathrm{j}f_k, \theta) - G(\mathrm{j}f_k) = \frac{B(\mathrm{j}f_k, \theta)}{A(\mathrm{j}f_k, \theta)} - G(\mathrm{j}f_k) \approx 0. \tag{5.4}$$

This Equation (5.4) is minimized with least squares approach.

Least squares minimization is typically used in linear case and it can be noted that Equation (5.4) is not linear in parameters. By multiplying Eq. (5.4) with the denominator polynomial $A(\mathrm{j}f_k, \theta)$ it becomes

$$E^{\mathrm{LS}}(\mathrm{j}f_k) = B(\mathrm{j}f_k, \theta) - A(\mathrm{j}f_k, \theta)G(\mathrm{j}f_k). \tag{5.5}$$

This linearization method was first presented by (Levy, 1959).

It should be noted that the parameter estimation Equation (5.5) overemphasizes the higher frequency components. Also considering that AMB system with current controller has a 40dB roll-off per decade, more accurate results can be achieved with using relative error rather than absolute error. This has been discussed in (Gähler, 1994b) and (Hynynen, 2011). Now a weighting function $W(\mathrm{j}f_k)$ is used to change Equation (5.5) in to a relative error problem and to minimize the overemphasis of the higher frequency components

$$W(\mathrm{j}f_k) = \frac{1}{A(\mathrm{j}f_k, \theta_{m-1})G(\mathrm{j}f_{\mathrm{k}})}, \tag{5.6}$$

where $A(\mathrm{j}f_{\mathrm{k}}, \theta_{\mathrm{m}-1})$ is the denominator coefficients of the previous parameter estimation. This leads to an iterative search of the least squares minimization of the Equation (5.5). Adding weight function $W(\mathrm{j}f_k)$ to Eq. (5.5) leads to following iterative least squares minimization problem

$$E^{\mathrm{LS}}(\mathrm{j}f_k) = \frac{B(\mathrm{j}f_{\mathrm{k}}, \theta_{\mathrm{m}}) - A(\mathrm{j}f_k, \theta_{\mathrm{m}})G(\mathrm{j}f_k)}{A(\mathrm{j}f_k, \theta_{m-1})G(\mathrm{j}f_k)} \tag{5.7}$$

and this leads to a weighted linear least-squares cost function $l_{\mathrm{LS}}(\theta)$

$$l_{\mathrm{LS}}(\theta) = \sum_{k=1}^{n_{\mathrm{f}}} \left| E^{\mathrm{LS}}(\mathrm{j}f_k) \right|^2 = \sum_{k=1}^{n_{\mathrm{f}}} \frac{|B(\mathrm{j}f_k,\theta_{\mathrm{m}}) - A(\mathrm{j}f_k,\theta_{\mathrm{m}})G(\mathrm{j}f_k)|^2}{|A(\mathrm{j}f_k,\theta_{\mathrm{m-1}})G(\mathrm{j}f_k)|^2}, \tag{5.8}$$

where n_{f} is the total number of frequencies.

Minimizing the cost function Eq. (5.8) leads to the parameter estimates. Least squares formulation based on Jacobian matrix $\boldsymbol{J}$ is used to solve the minimization of Eq. (5.8). Equation (5.8) is reformulated as (Hynynen, 2011)

$$E^{\mathrm{LS}}(\mathrm{j}f_k) = \boldsymbol{J}\boldsymbol{\theta} = 0, \tag{5.9}$$

where $\boldsymbol{\theta}$ is the parametric vector containing values of transfer function polynomial coefficients b_j and a_j. Equation (5.9) can be formulated as (Verboven, 2002)

$$E^{\mathrm{LS}}(\mathrm{j}f_{\mathrm{k}}) = [\boldsymbol{\Gamma}\ \boldsymbol{\Phi}] \begin{bmatrix} \boldsymbol{\theta}_b \\ \boldsymbol{\theta}_{\boldsymbol{a}} \end{bmatrix} \approx 0, \tag{5.10}$$

where submatrices **Γ** and **Φ** can be determined as

$$\boldsymbol{\Gamma} = \begin{bmatrix} \boldsymbol{\Gamma}(\mathrm{j}f_1) \\ \boldsymbol{\Gamma}(\mathrm{j}f_2) \\ \vdots \\ \boldsymbol{\Gamma}(\mathrm{j}f_{n_{\mathrm{f}}}) \end{bmatrix} \text{ and} \tag{5.11}$$

$$\boldsymbol{\Phi} = \begin{bmatrix} \boldsymbol{\Phi}(\mathrm{j}f_1) \\ \boldsymbol{\Phi}(\mathrm{j}f_2) \\ \vdots \\ \boldsymbol{\Phi}(\mathrm{j}f_{n_{\mathrm{f}}}) \end{bmatrix}, \text{ where} \tag{5.12}$$

$$\boldsymbol{\Gamma}(\mathrm{j}f_k) = \boldsymbol{W}(\mathrm{j}f_k)[(\mathrm{j}f_k)^0 \quad (\mathrm{j}f_k)^1 \quad \ldots \quad (\mathrm{j}f_k)^n], \tag{5.13}$$

$$\boldsymbol{\Phi}(\mathrm{j}f_{\mathrm{k}}) = -\boldsymbol{\Gamma}(\mathrm{j}f_k)\, G(\mathrm{j}f_k), \tag{5.14}$$

$$\boldsymbol{\theta}_a = \begin{bmatrix} \mathrm{a}_0 \\ \mathrm{a}_1 \\ \vdots \\ \mathrm{a}_{\boldsymbol{n}} \end{bmatrix}, \boldsymbol{\theta}_b = \begin{bmatrix} \mathrm{b}_0 \\ \mathrm{b}_1 \\ \vdots \\ \mathrm{b}_{\boldsymbol{n}} \end{bmatrix} \text{ and } \boldsymbol{\theta} = \begin{bmatrix} \boldsymbol{\theta_b} \\ \boldsymbol{\theta}_{\mathrm{a}} \end{bmatrix} = \begin{bmatrix} \mathrm{b}_{\boldsymbol{0}} \\ \vdots \\ \mathrm{b}_{\boldsymbol{n}} \\ \mathrm{a}_{\boldsymbol{0}} \\ \vdots \\ \mathrm{a}_n \end{bmatrix}. \tag{5.15}$$

Number of rows of the Jacobian matrix $\boldsymbol{J}$ is the value of total frequencies n_f and number of columns is 2*(n+1), where n is the order of the transfer function. If parameter values are solved directly from Equation (5.10), this matrix can be very large and much computational effort is needed to solve it assuming $n_\mathrm{f} \gg n$. Often parameters are solved by using 'normal equations' instead, which reduces the size of the Jacobian matrix (Verboven, 2002). Equation (5.8) is written using normal equations as

$$l_{\mathrm{LS}}(\boldsymbol{\theta}) = \boldsymbol{\theta}^{\mathrm{T}}(\boldsymbol{J}^{\mathrm{H}}\boldsymbol{J})\boldsymbol{\theta}, \tag{5.16}$$

where $\boldsymbol{J}^{\mathrm{H}}\boldsymbol{J}$ can be written as

$$\boldsymbol{J}^{\mathrm{H}}\boldsymbol{J} = \begin{bmatrix} \boldsymbol{\Gamma}^{\mathrm{H}}\boldsymbol{\Gamma} & \boldsymbol{\Gamma}^{\mathrm{H}}\boldsymbol{\Phi} \\ \boldsymbol{\Phi}^{\mathrm{H}}\boldsymbol{\Gamma} & \boldsymbol{\Phi}^{\mathrm{H}}\boldsymbol{\Phi} \end{bmatrix}. \tag{5.17}$$

It can be seen that the number of rows of this matrix is 2*(n+1) and is also the number of columns. We have successfully eliminated the number of frequencies n_f from the number of rows.

Defining submatrices of Equation (5.17) with (Hynynen, 2011)

$$\boldsymbol{R} = \boldsymbol{\Gamma}^{\mathrm{H}}\boldsymbol{\Gamma}, \tag{5.18}$$

$$\boldsymbol{S} = \boldsymbol{\Gamma}^{\mathrm{H}}\boldsymbol{\Phi} \text{ and} \tag{5.19}$$

$$\boldsymbol{T} = \boldsymbol{\Phi}^{\mathrm{H}}\boldsymbol{\Phi}, \tag{5.20}$$

normal equation is written as

$$\begin{bmatrix} \boldsymbol{R} & \boldsymbol{S} \\ \boldsymbol{S}^{\mathrm{H}} & \boldsymbol{T} \end{bmatrix} \begin{bmatrix} \boldsymbol{\theta}_b \\ \boldsymbol{\theta}_a \end{bmatrix} \approx 0. \tag{5.21}$$

Minimizing the cost function of Eq. (5.21) in relation to the unknown parameters $\boldsymbol{\theta}_b$ and $\boldsymbol{\theta}_a$ leads to the following partial derivations (Hynynen, 2011)

$$\frac{\partial l_{\mathrm{LS}}(\theta)}{\partial \boldsymbol{\theta}_{\mathrm{b}}} = 2(\boldsymbol{R}\boldsymbol{\theta}_b + \boldsymbol{S}\boldsymbol{\theta}_a) \text{ and} \tag{5.22}$$

$$\frac{\partial l_{LS}(\theta)}{\partial \boldsymbol{\theta}_a} = 2(\boldsymbol{S}^{\mathrm{H}}\boldsymbol{\theta}_b + \boldsymbol{T}\boldsymbol{\theta}_a) = 0. \tag{5.23}$$

Solving Equation (5.22) in respect to $\boldsymbol{\theta}_b$ yields

$$\boldsymbol{\theta}_b = -\boldsymbol{R}^{-1}\boldsymbol{S}\boldsymbol{\theta}_{\boldsymbol{a}}, \tag{5.24}$$

and substituting $\boldsymbol{\theta}_b$ solved in Eq. (5.24) to Equation (5.23) leads to

$$[\boldsymbol{T} - \boldsymbol{S}^{\mathrm{H}}\boldsymbol{R}^{-1}\boldsymbol{S}]\boldsymbol{\theta}_{\mathrm{a}} = \boldsymbol{D}\boldsymbol{\theta}_{\mathrm{a}} \approx 0. \tag{5.25}$$

Denominator polynomial coefficients $\boldsymbol{\theta}_{\mathrm{a}}$ can be solved from Eq. (5.25) with for example fixing the highest order coefficient $\mathrm{a_n}$ to 1 and calculating the other coefficients with (Verboven, 2002)

$$\boldsymbol{\theta}_{\mathrm{a_{LS}}} = \begin{Bmatrix} -[\boldsymbol{D}(1\!:\!n, 1\!:\!n)]^{-1}\{\boldsymbol{D}(1\!:\!n, n+1)\} \\ 1 \end{Bmatrix}. \tag{5.26}$$

Numerator polynomial coefficients $\boldsymbol{\theta}_b$ are then calculated from Eq. (5.24). Now the transfer function can be written with obtained numerator $\boldsymbol{\theta}_b$ and denominator $\boldsymbol{\theta}_{\mathrm{a}}$

$$\hat{G}(s) = \frac{b_n s^n + b_{n-1}s^{n-1} + \cdots + b_0}{s^n + a_{n-1}s^{n-1} + \cdots + a_0}. \tag{5.27}$$

Pole- and zero-frequencies can be extracted from identified transfer function $\hat{G}(\mathrm{s})$. Pole frequencies are named as resonance frequencies and zero frequencies are named as anti-resonance frequencies. In this case they are extracted with MATLAB® functions pole and zero. With pole and zero functions also resonance and anti-resonance damping ratios are extracted.

5.2 Rotor model update method

FEM-model of the rotor presented in Chapter 2.2 is still only an approximation of the real rotor. Real rotors in high-speed applications have complex nature and are constructed from number of different elements. Shrink fit is usually used to connect them and that leads to quite different properties of elements when describing them through Timoshenko theory. The other source of uncertainty is the stiffness of the laminations as it consists of many thin parts and the final stiffness is defined by the pressure which keeps the stack together. In addition active part

of the electrical machine might have a complex geometry such as slits or surface mounted or embedded permanent magnets. These components are selected as uncertain, however the axle which is usually a solid piece is well defined with the beam theory. To correct the FEM-model based on identification data authors in (Wróblewski, 2011) presented a method which uses resonance and anti-resonance frequency information from experimental data and model. This method was extended to use damping ratios also in the resonance and anti-resonance frequencies.

This method is used to tune the selected elements elasticity value e_p from the FEM-model until an acceptable solution is found. Number of elements can be selected freely. Other elements elasticity values were assumed to be correct and remained at the fixed nominal value. With all selected elasticity values e_p, design variable vector $\boldsymbol{e}$ can be formulated (Wróblewski, 2011)

$$\boldsymbol{e} \in \mathbb{R}^{\boldsymbol{n}} \text{ so that } \{e_p\}_{p=1\ldots n}, \tag{5.28}$$

where *n* is the number of design values. This vector $\boldsymbol{e}$ is used to calculate the new model based on changed elasticity values e_p.

After a new model is obtained with design variable vector $\boldsymbol{e}$, resonance and anti-resonance frequencies are extracted for the selected axes from the new model and are compared to the resonance and anti-resonance frequencies obtained from experimental data with method presented in Chapter 5.1. Damping ratios are also extracted from the experimental data and model data in the resonance and anti-resonance frequencies and are compared. Variable $f_{ij,k}^{\mathrm{r,E}}$ is used to represent the frequency resonance error and $f_{ij,k}^{\mathrm{a,E}}$ is used to represent the anti-resonance frequency error. Relative frequency errors can be calculated with (adapted from Wróblewski, 2011)

$$f_{ij,k}^{\mathrm{r,E}} = \frac{\left|\hat{\omega}_{ij,k}^{\mathrm{r}} - \tilde{\omega}_{ij,k}^{\mathrm{r}}\right|}{\hat{\omega}_{ij,k}^{\mathrm{r}}} \text{ and} \tag{5.29}$$

$$f_{ij,k}^{\mathrm{a,E}} = \frac{\left|\hat{\omega}_{ij,k}^{\mathrm{a}} - \tilde{\omega}_{ij,k}^{\mathrm{a}}\right|}{\hat{\omega}_{ij,k}^{\mathrm{a}}}, \tag{5.30}$$

where $\hat{\omega}_{ij,k}^{\mathrm{r}}$ is the experimental resonance frequency and $\tilde{\omega}_{ij,k}^{\mathrm{r}}$ is the resonance frequency obtained from model. $\hat{\omega}_{ij,k}^{\mathrm{a}}$ is the anti-resonance frequency from experimental data and $\tilde{\omega}_{ij,k}^{\mathrm{a}}$ is the anti-resonance frequency obtained from model. For damping ratios $d_{ij,k}^{\mathrm{r,E}}$ is used to represent the damping ratio error in resonance frequency and $d_{ij,k}^{\mathrm{a,E}}$ is used to represent the damping ratio error in anti-resonance frequency. Relative damping ratio errors can be calculated with

$$d_{ij,k}^{\mathrm{r,E}} = \frac{\left|\hat{\zeta}_{ij,k}^{\mathrm{r}} - \tilde{\zeta}_{ij,k}^{\mathrm{r}}\right|}{\hat{\zeta}_{ij,k}^{\mathrm{r}}} \text{ and} \tag{5.31}$$

$$d_{ij,k}^{\mathrm{a,E}} = \frac{\left|\hat{\zeta}_{ij,k}^{\mathrm{a}} - \tilde{\zeta}_{ij,k}^{\mathrm{a}}\right|}{\hat{\zeta}_{ij,k}^{\mathrm{a}}}, \tag{5.32}$$

where $\hat{\zeta}_{ij,k}^{\mathrm{r}}$ is the damping ratio from experimental resonance frequency and $\tilde{\zeta}_{ij,k}^{\mathrm{r}}$ is the damping ratio from model resonance frequency. $\hat{\zeta}_{ij,k}^{\mathrm{a}}$ is the damping ratio from experimental anti-resonance frequency and $\tilde{\zeta}_{ij,k}^{\mathrm{a}}$ is the damping ratio from model anti-resonance frequency.

Subscripts *i* and *j* represent the excitation input and output axis and *k* represents the resonance/anti-resonance peak index number. Relation between subscripts *i* and *j* is presented in Table 5.1.

Table 5.1. Relation between excitation input and output axis of the subscripts *i* and *j*.

Input (i)/Output (j)	NX(1)	NY(2)	DX(3)	DY(4)
NX(1)	11	12	13	14
NY(2)	21	22	23	24
DX(3)	31	32	33	34
DY(4)	41	42	43	44

In this thesis only excitations in *x*-direction on the same input and output axis are considered. So *i* and *j* pairs (11) and (33) are used.

After adding resonance frequency weight $w_{\mathrm{f},k}^{\mathrm{r}}$ and anti-resonance frequency weight $w_{\mathrm{f},k}^{\mathrm{a}}$ to equations (5.29) and (5.30) total frequency error function can be written as (adapted from Wróblewski, 2011)

$$err_{\mathrm{f}}\left(f_{ij,k}^{\mathrm{r,E}}, f_{ij,k}^{\mathrm{a,E}}\right) = \sum_{i=1}^{b_{\mathrm{x}}} \sum_{j=1}^{b_{\mathrm{y}}} \sum_{k=1}^{\mathrm{m}_f} \left[w_{\mathrm{f},k}^{\mathrm{r}} * f_{ij,k}^{\mathrm{r,E}} + w_{\mathrm{f},k}^{\mathrm{a}} * f_{ij,k}^{\mathrm{a,E}}\right], \tag{5.33}$$

where b_{x} and b_{y} are the dimension selected from Table 5.1 and m_{f} is the number flexible modes used. Weights can be selected by the need of prioritizing some resonance and/or anti-resonance frequency errors over one other.

Weights are also added to the damping ratio errors. Resonance damping ratio weight is marked as $w_{\mathrm{d},k}^{\mathrm{r}}$ and anti-resonance damping ratio is marked as $w_{\mathrm{d},k}^{\mathrm{a}}$. These weights are then added to equations (5.31) and (5.32) providing the following total damping ratio error function

$$err_{\mathrm{d}}\left(d_{ij,k}^{\mathrm{r,E}}, d_{ij,k}^{\mathrm{a,E}}\right) = \sum_{i=1}^{b_{\mathrm{x}}} \sum_{j=1}^{b_{\mathrm{y}}} \sum_{k=1}^{m_f} \left[w_{\mathrm{d},k}^{\mathrm{r}} * d_{ij,k}^{\mathrm{r,E}} + w_{\mathrm{d},k}^{\mathrm{a}} * d_{ij,k}^{\mathrm{a,E}}\right]. \tag{5.34}$$

A total error function can be formulated with summing Eq. (5.33) and (5.34)

$$err_{\mathrm{tot}} = err_{\mathrm{f}} + w_{\mathrm{d}} * err_{\mathrm{d}}, \tag{5.35}$$

where w_{d} is a weight used to decrease the effect of total damping ratio error in the total error calculation an thus is smaller than 1. When the error function presented in Eq. (5.35) is close to zero, model obtained with design variable vector $\boldsymbol{e}$ corresponds satisfactory to the experimental data. This is the function to be minimized with the rotor model updating method.

A black box function $B(\boldsymbol{e})$ is used to describe the process of determining the model based on value of design variable vector $\boldsymbol{e}$ and outputting a single error value from Eq. (5.35) after determining resonance and anti-resonance frequencies and damping ratios from model and using experimental data. Now the function to be minimized can be generalized as (Wróblewski, 2011)

$$\min_{\boldsymbol{e}\in\mathbb{R}^n} B(\boldsymbol{e}). \tag{5.36}$$

Minimization of Eq. (5.36) was done with Nelder-Mead function minimization method (Nelder, 1965). Design variable vector $\boldsymbol{e}$ is altered until an acceptable minimum is found. Nelder-Mead optimization method is a derivate free method and only uses the current function values. Minimum is found with iterative steps by updating the simplex vertices with reflection, expansion, contradiction or reduction. This optimization method was selected, because it is easy to implement and is derivative free. Figure 5.1 shows the flow chart of rotor model updating operation.

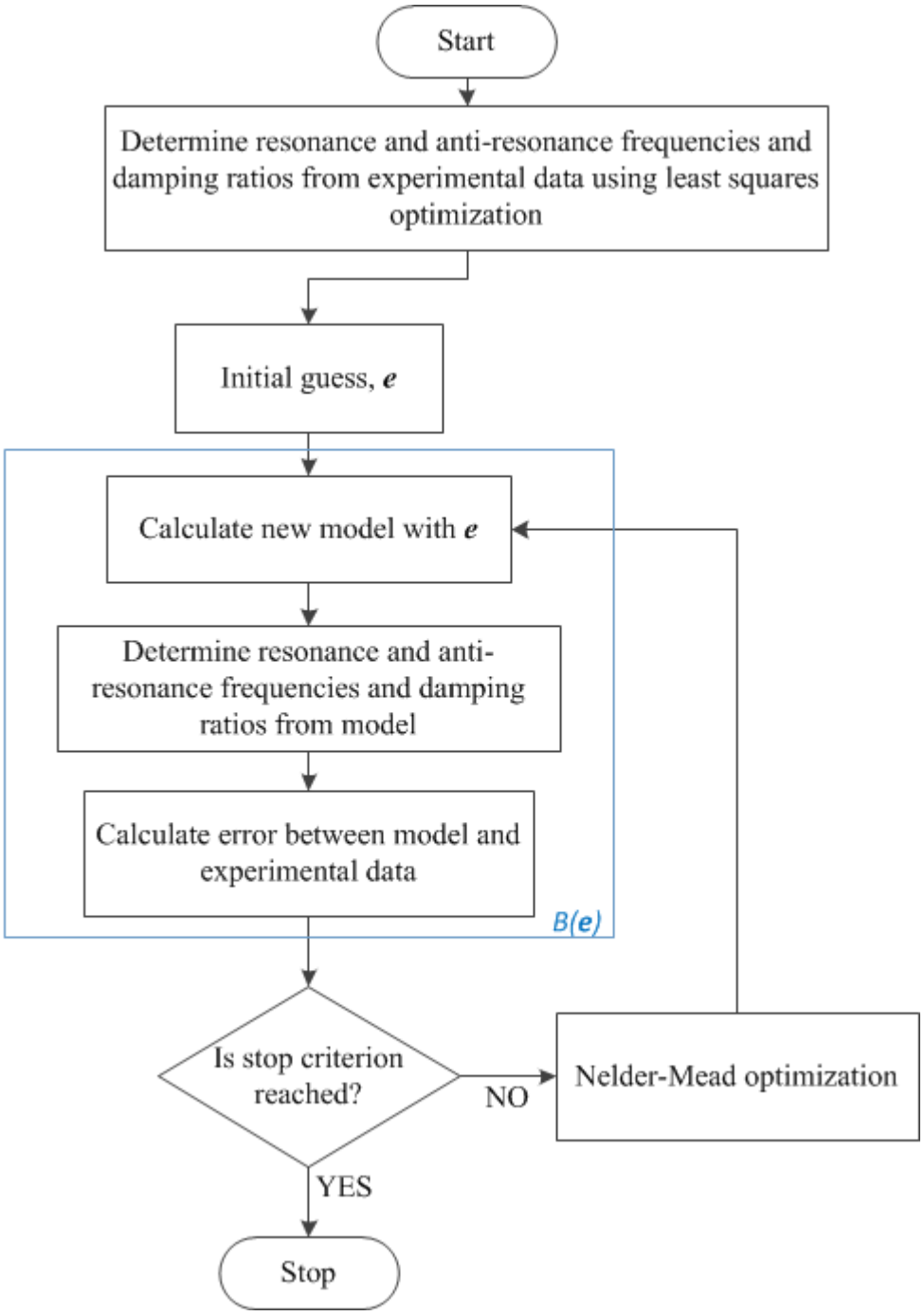

Fig. 5.1. Flow chart of the rotor model updating method.

Some consideration with starting design values e_p might be needed, because Nelder-Mead optimization might lead to a local minimum. Because e_p values represent elasticity of the

material they are constrained to be greater than zero. Also a maximum value could be used to constrain e_p values.

A MATLAB® script was developed for updating the rotor model. This script is shown in appendix 1. The rotor model is updated based on method presented above.

5.3 Demonstration of rotor model update method

A simple reference rotor model consisting of 20 equal beam elements was constructed. Elasticity of elements 5-8 was altered and these values e_p were used as design variables. The first resonance and anti-resonance frequency and damping ratios were used. Excitations in the *x*-direction on the same input and output axis were considered (NX and DX). Figure 5.2 shows the reference case rotor model.

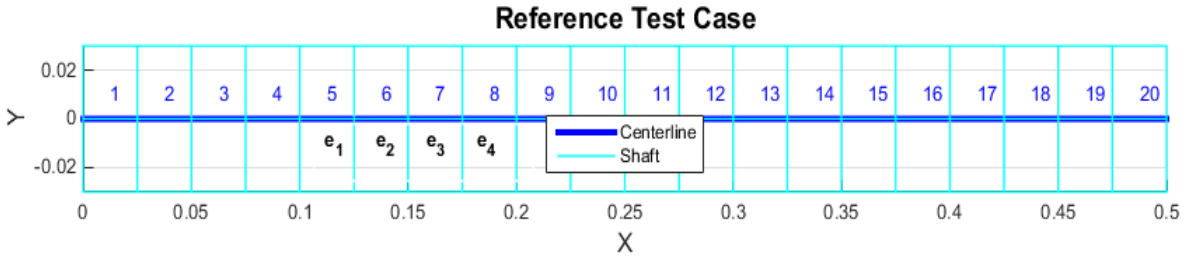

Fig. 5.2. Reference case rotor model showing the locations of the design variables e_p. Blue number shows the element number.

After randomizing the elasticity values e_p of the original model, reference and original model's resonance and anti-resonance frequencies and damping ratios are compared. In this case elasticity values e_p of the original model are: e_1 is 107.7 GPa, e_2 is 80.1 GPa, e_3 is 41.1 GPa and e_4 is 18.9 GPa. Table 5.2 shows comparison between original model and reference model.

Table 5.2. Comparison between reference and original model's resonance and anti-resonance frequencies and damping ratios.

Feature of interest	Reference model	Original model	Absolute error	Error %
NX(1,1) first resonance frequency	733.37 Hz	672.21 Hz	62.159 Hz	8.48
NX(1,1) first anti-resonance frequency	544.45 Hz	495.98 Hz	48.47 Hz	8.90
DX(3,3) first resonance frequency	733.37 Hz	671.21 Hz	62.159 Hz	8.48
DX(3,3) first anti-resonance frequency	640.18 Hz	588.83 Hz	51.350 Hz	8.02
NX(1,1) first resonance damping ratio	0.0020039	0.0020047	$7.8941 * 10^{-7}$	0.0394
NX(1,1) first anti-resonance damping ratio	0.0014769	0.0014711	$5.8547 * 10^{-6}$	0.396
DX(3,3) first resonance damping ratio	0.0020039	0.0020047	$7.8941 * 10^{-7}$	0.0394
DX(3,3) first anti-resonance damping ratio	0.0017462	0.001756	$9.7378 * 10^{-6}$	0.558

A bode plot can be used to show the difference between original and reference model. Figure 5.3 shows the bode plot of NX- and DX-axes between original and reference model.

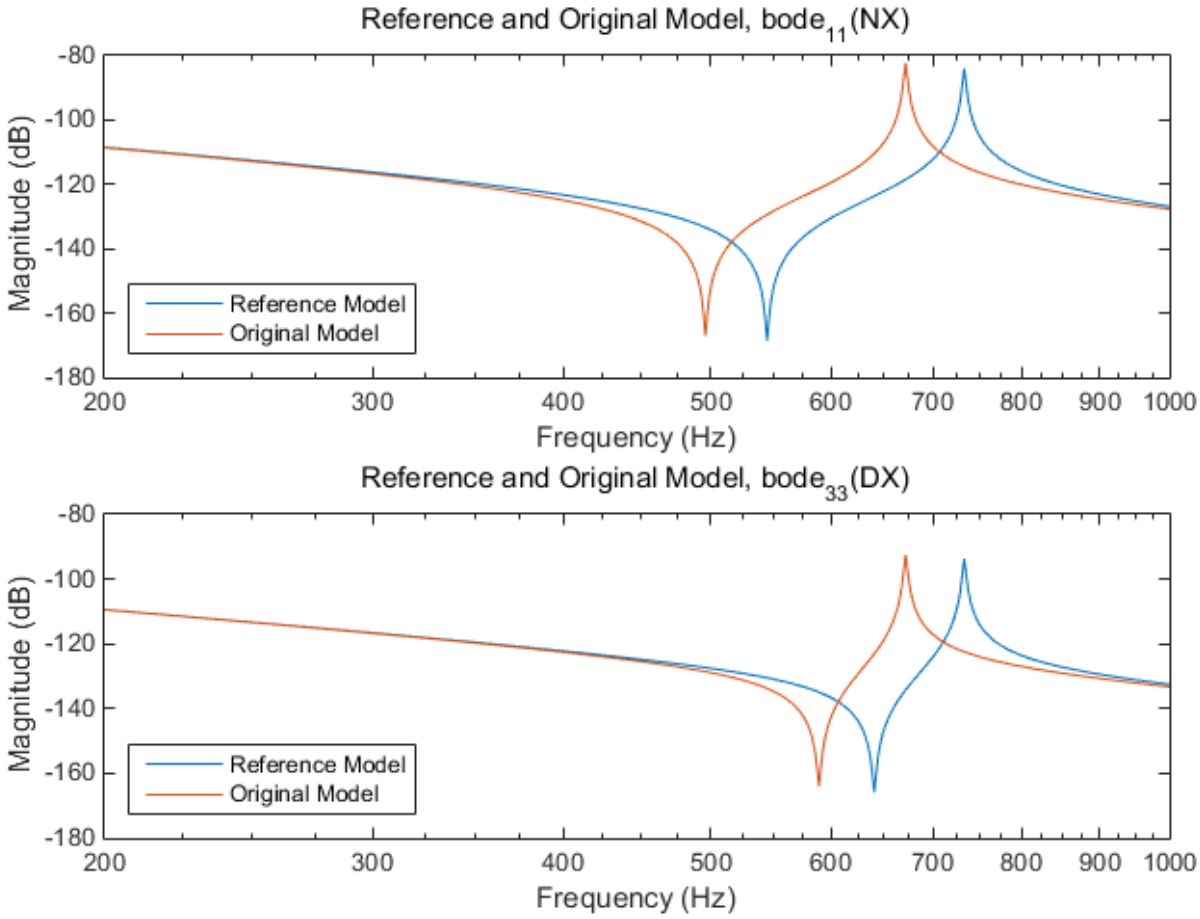

Fig. 5.3. Bode plot of the NX- and DX-axes between reference and original model.

As can be seen from Fig. 5.3 and Table 5.2, there is a significant difference between the original and reference model. Thus there is a need to update the original model.

Original model was updated with the method presented in Chapter 5.2. Weights for resonance frequency $w_{\mathrm{f},k}^{\mathrm{r}}$, anti-resonance frequency $w_{\mathrm{f},k}^{\mathrm{a}}$, resonance frequency damping ratio $w_{\mathrm{d},k}^{\mathrm{r}}$ and anti-resonance frequency damping ratio $w_{\mathrm{d},k}^{\mathrm{a}}$ were assumed to be 1. Weight w_{d} used to decrease the effect of total damping ratio error in the total error was 0.01. Updated model was then compared with the reference model. This comparison is shown in Table 5.3.

Table 5.3. Comparison of resonance and anti-resonance frequencies and damping ratios between reference and updated model.

Feature of interest	Reference model	Updated model	Absolute error	Error %
NX(1,1) first resonance frequency	733.37 Hz	733.37 Hz	≈ 0 Hz	≈ 0
NX(1,1) first anti-resonance frequency	544.45 Hz	544.45 Hz	≈ 0 Hz	≈ 0
DX(3,3) first resonance frequency	733.37 Hz	733.37 Hz	≈ 0 Hz	≈ 0
DX(3,3) first anti-resonance frequency	640.18 Hz	640 Hz	0.18165 Hz	0.0284
NX(1,1) first resonance damping ratio	0.0020039	0.0020039	≈ 0	≈ 0
NX(1,1) first anti-resonance damping ratio	0.0014769	0.0014766	$3.2661 * 10^{-7}$	0.0221
DX(3,3) first resonance damping ratio	0.0020039	0.0020039	≈ 0	≈ 0
DX(3,3) first anti-resonance damping ratio	0.0017462	0.0017458	$4.6865 * 10^{-7}$	0.0268

In this case a bode plot is also used to compare reference and updated model. Bode plots of the NX- and DX-axes are shown in Figure 5.4.

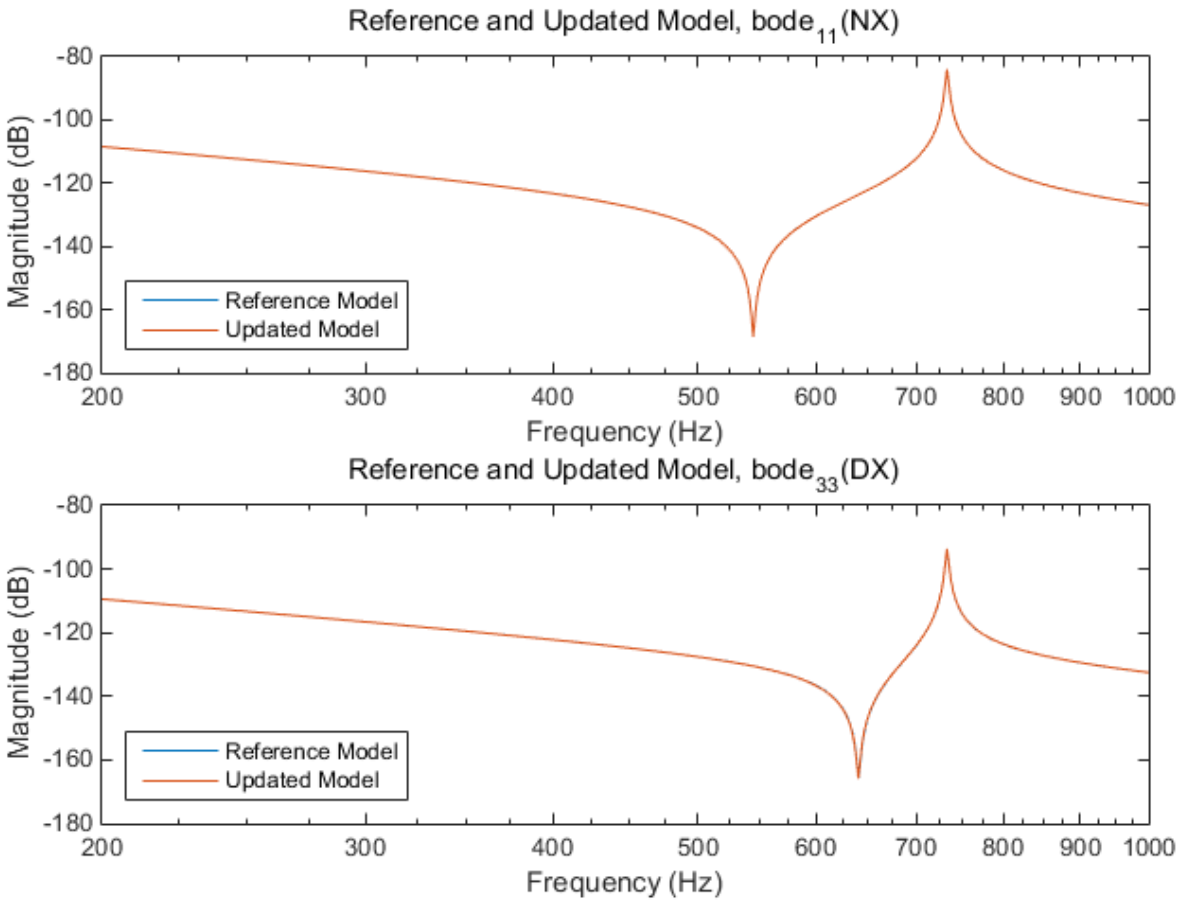

Fig. 5.4. Bode plot of the reference and updated model's NX- and DX-axes. Curves from both axes are overlapping each other.

As can be seen from Fig. 5.4 where plots from both NX- and DX-axes between reference and updated model are on top of each other, there seems to be no difference between reference and updated model. Looking at Table 5.3 there is a very small error between updated and reference model's resonance and anti-resonance frequencies. A bit bigger error can be seen between damping ratio errors and the cause of this is the selected weights. Now the correspondence between reference and the updated model is satisfactory. Figure 5.5 shows the updated elasticity values e_p from updated model.

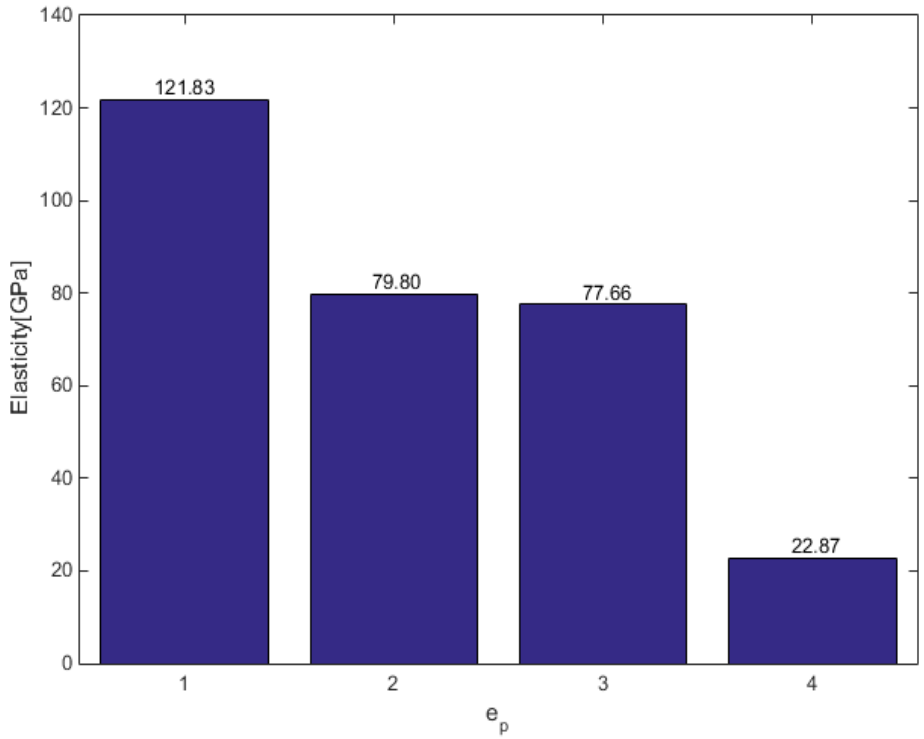

Fig. 5.5. Elasticity values e_p from the updated model. In the original model elasticity value of e_1 was 107.7 GPa, e_2 was 80.1 GPa, e_3 was 41.1 GPa and e_4 was 18.9 GPa.

In conclusion, with the rotor model update method presented in Ch. 5.2 an updated model describing more accurately the reference model was obtained. Update procedure with four design variables e_p ran at about 11.5 iterations per second.

6 EXPERIMENTS AND RESULTS

In this chapter test results are presented from magnetic center calibration presented in Chapter 3, rotor model identification presented in Chapter 4 and rotor model update method presented in Chapter 5. Test machine used was HS-Eden machine, which has two radial active magnetic bearings and one axial active magnetic bearing. Radial AMB structure is an E-core structure which has 12 poles but with some assumptions it is approximated with a standard eight pole bearing. Figure 6.1 shows the structure of the E-core bearing.

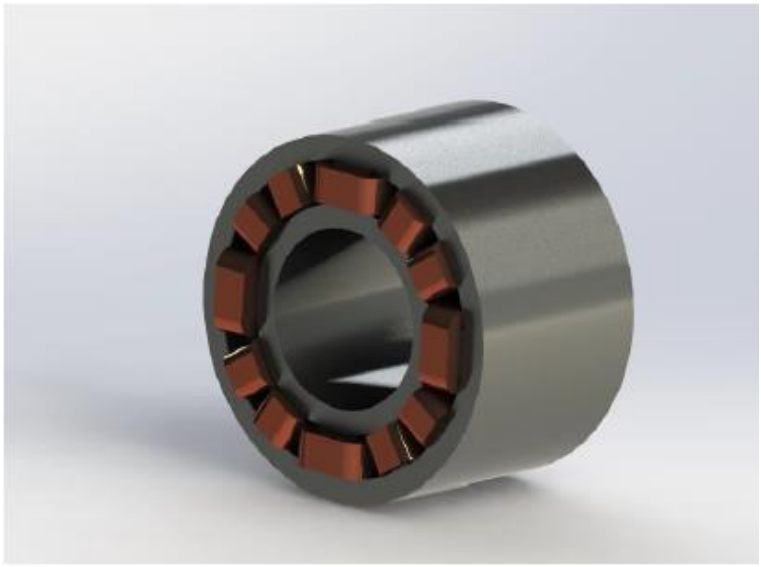

Fig. 6.1. E-core AMB (Smirnov, 2015).

6.1 Rotor magnetic center calibration

Magnetic center of the rotor was determined for the HS-Eden machine with the algorithm developed in Ch. 3.3. The nominal bias current i_{b} was 5 A so following bias current values were used

1. 4.0 A
2. 4.5 A
3. 5.0 A
4. 5.5 A
5. 6.0 A.

From these bias current values ten bias current pairs were used

1. 4.0 A and 4.5 A
2. 4.0 A and 5.0 A
3. 4.0 A and 5.5 A
4. 4.0 A and 6.0 A
5. 4.5 A and 5.0 A
6. 4.5 A and 5.5 A
7. 4.5 A and 6.0 A
8. 5.0 A and 5.5 A
9. 5.0 A and 6.0 A
10. 5.5 A and 6.0 A.

Iteration limit was 15 iterations per bias current pair and the stopping criterion used for the rotor position offset $x_{\mathrm{c},n}$ was ± 3 µm. Magnetic center was identified for all radial axes (DX, DY, NX, NY). Figure 6.2 shows the rotor position of pair number 1 of the magnetic center identification. Table 6.1 shows the related rotor position offsets.

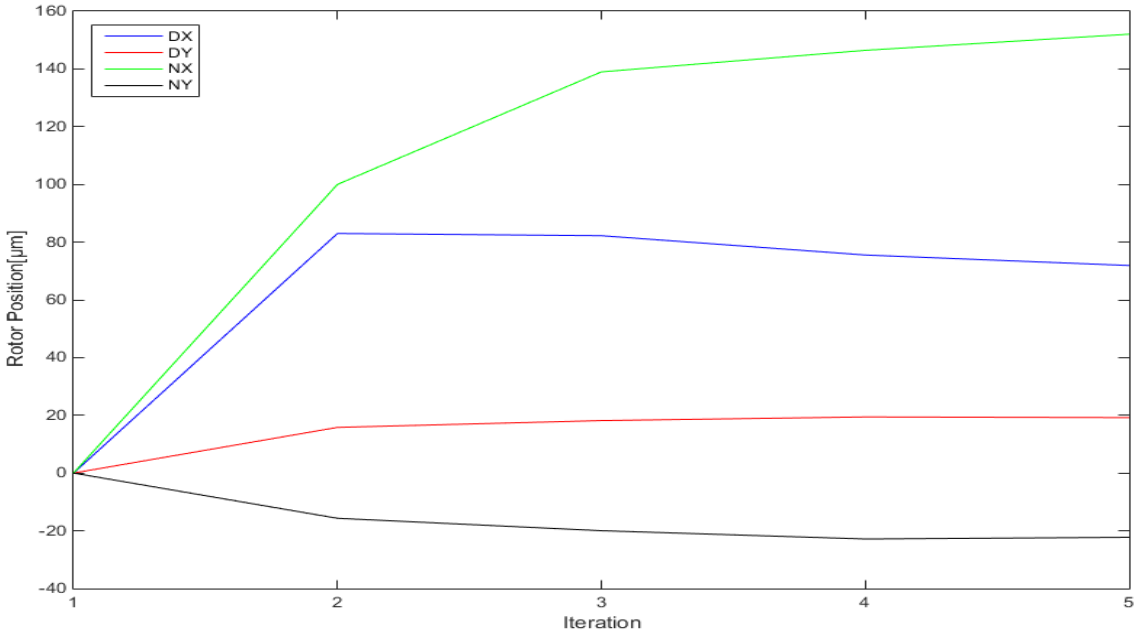

Fig. 6.2. Rotor position from pair number 1 of the magnetic center identification.

Table 6.1. Rotor position offsets from pair 1 of the magnetic center identification.

Iteration	DX-position offset [µm]	DY-position offset [µm]	NX-position offset [µm]	NY-position offset [µm]
1	-83.00	-15.82	-100.00	15.67
2	0.77	-2.36	-38.98	4.30
3	6.69	-1.26	-7.47	2.87
4	3.64	0.23	-5.59	-0.58
5	-1.19	1.52	-2.41	0.72

As can be seen from Table 6.1 all the position offsets from all axes converge very rapidly to between ± 3 µm. Only five iterations were needed to achieve this accuracy. In Table 6.2 one magnetic center calibration of the rotor is shown with all temporary rotor position values of the ten bias current pairs.

Table 6.2. Rotor position with the bias current pairs from one magnetic center calibration.

Bias current pair	DX-position [µm]	DY-position [µm]	NX-position [µm]	NY-position [µm]
1	73.99	19.48	151.61	-22.98
2	73.35	15.26	150.19	-20.91
3	71.15	13.59	152.71	-20.15
4	69.73	9.65	149.93	-20.95
5	75.43	15.27	150.54	-16.90
6	70.00	10.51	153.61	-16.91
7	69.56	8.67	150.21	-19.27
8	72.35	9.42	154.98	-14.21
9	69.68	8.41	151.01	-18.39
10	68.97	5.54	148.62	-20.42
Average	71.42	11.58	151.34	-19.11

From Table 6.2 it can be seen, that by using ten different bias current pairs an accurate average is obtained. Largest variation of position is from DY-axis where variation is about 14 µm. In the other axes variation is less than 8.8 µm. Repeatability of the magnetic center identification is demonstrated in Table 6.3. Magnetic center calibration was repeated five times.

Table 6.3. Repeatability of the magnetic center calibration.

Repetition	DX-position [µm]	DY-position [µm]	NX-position [µm]	NY-position [µm]
1	70.57	9.75	146.33	-21.55
2	69.47	9.98	148.78	-21.24
3	70.81	10.4	148.78	-20.72
4	71.35	11.18	149.48	-19.96
5	71.29	11.12	149.95	-19.76
Average	70.7	10.49	148.66	-20.65

From Table 6.3 it can be seen that the repeatability of the magnetic center calibration is very high and that the values between different repetitions do not differ much. Variation is less than 3.7 µm for all axes between these five repetitions. For the repeatability testing it should be noted, that the rotor should be kept in the exact same position between repeatability tests, because sensor runout might cause the magnetic center calibration to end up in a very different location. Magnetic center of the HS-Eden machine is then located approximately at (70.7, 10.49, 148.66, -20.65) µm from the geometric center.

6.2 Stepped-sine identification of the rotor model

Rotor model of the HS-Eden machine was identified with the algorithm developed in Chapter 4.2. Frequency range of radial axes (DX, DY, NX, NY) identification was from 1 Hz up to 750 Hz containing 250 points between these frequencies. Frequency resolution is then 3.008 Hz. Figure 6.3 shows the bode plots from radial axes.

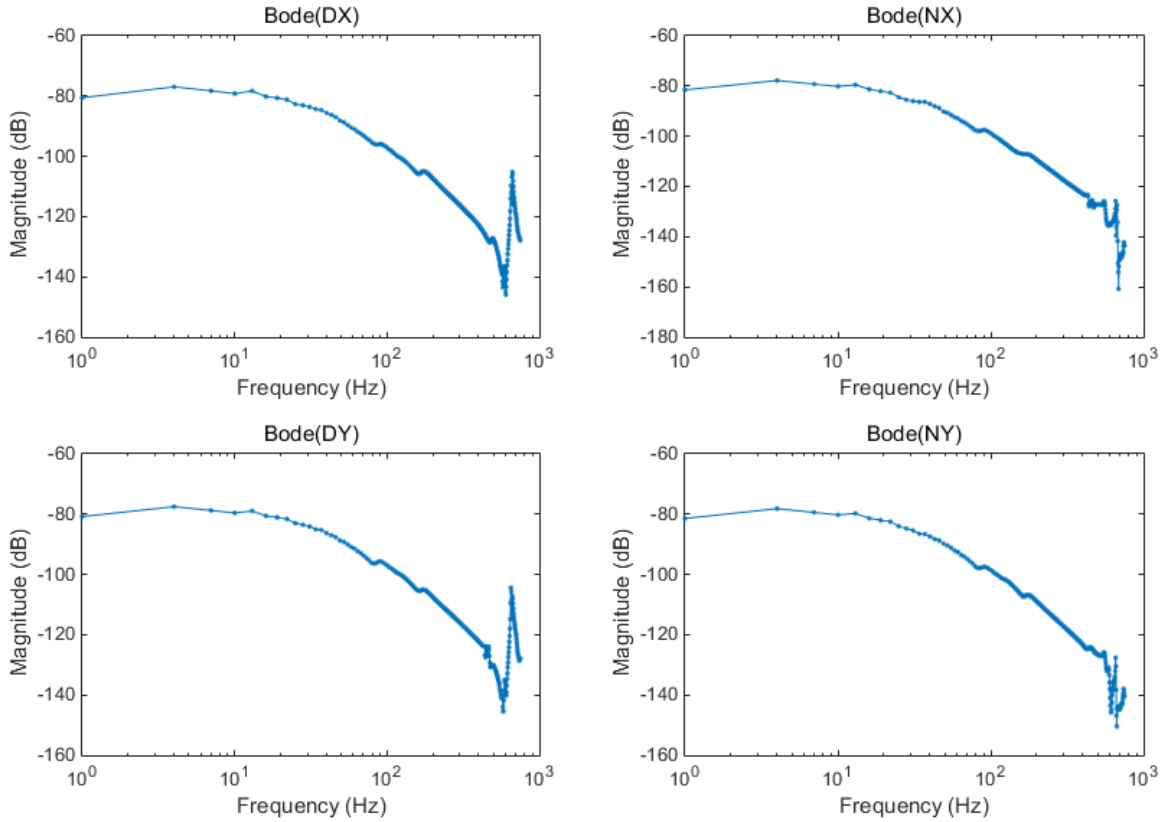

Fig. 6.3. Bode plots from radial axes of the HS-Eden machine rotor model identification. Dot in the plot indicates a measurement point.

From the bode plots shown in Fig. 6.3 the first flexible mode is clearly seen on all axes between 600…700 Hz. All radial axes also seem to behave similarly, in frequency range below 300 Hz which is expected, because they identify the same rotor, but from different axes. For the Z-axis identification frequency range was from 1 Hz up to 100 Hz containing 100 points between these frequencies. Frequency is resolution is thus 1 Hz. Bode plot from the Z-axis is shown in Figure 6.4.

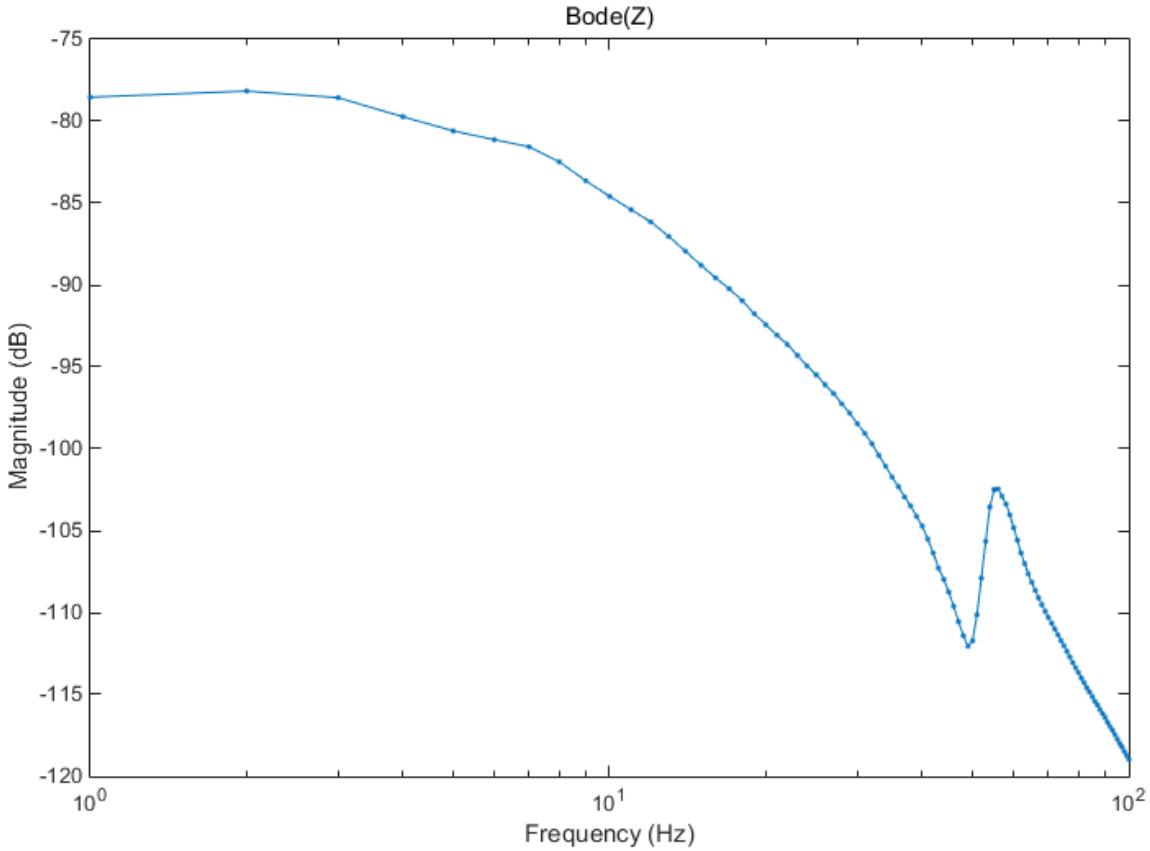

Fig. 6.4. Bode plot from Z-axis identification of the HS-Eden machine. Dot in the plot indicates a measurement point.

The measured results in Fig. 6.3 and 6.4 present small deviations at certain frequencies that might be a result of foundation resonances, switching power amplifier nature or DC-link voltage variation (Jastrzebski, 2012). In general these discrepancies can be neglected.

6.3 Rotor model update based on identification

Rotor model of the HS-Eden machine was updated with the method presented in Ch. 5.2. In this case first resonance and anti-resonance frequencies and damping ratios were used. Excitations for *x*-direction on the same input and output axis were considered (NX and DX) for the rotor model update. Parametric model of the rotor was constructed with the method shown in Ch. 5.1 based on experimental data obtained with the rotor model identification.

Resonance and anti-resonance frequencies and damping ratios related to the experimental data were then extracted from the parametric model. Resonance and anti-resonance frequencies and damping ratios from experimental data are shown later in Table 6.4. Design variables e_p were located at the outer part of the first radial AMB (1…4), outer part of the second radial AMB (5…8), and in the electrical machine part (9…14). These outer parts of the AMBs are considered as a ring. Outer parts of the AMBs were selected as design variables, because of the uncertainty of the stiffness of the laminations. Electrical machine part was selected, because it has a complex geometry. All elements nominal elasticity value was 200 GPa. Rotor model of the HS-Eden machine is shown in Fig 6.5.

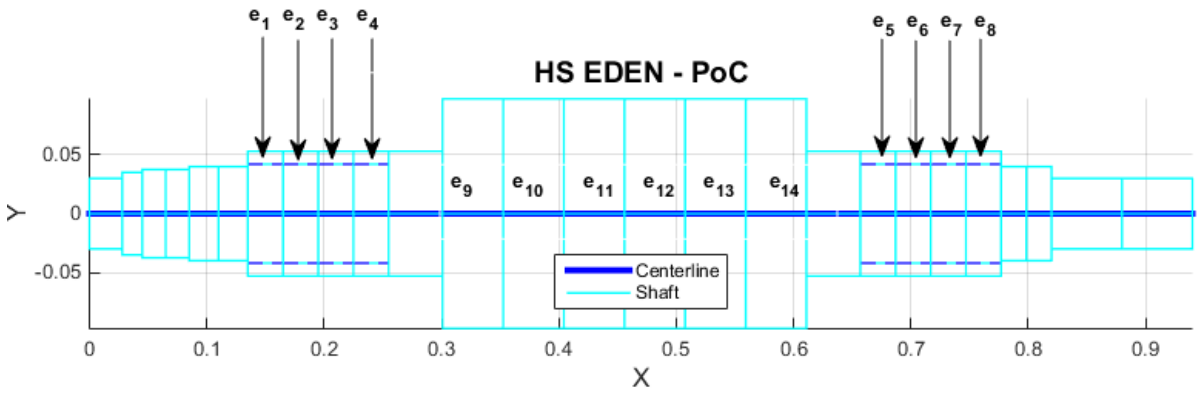

Fig. 6.5. Rotor model of the HS-Eden machine showing the locations of the design variables e_p.

Experimental data is then compared with the original model. This comparison is shown in Table 6.4.

Table 6.4. Comparison of the experimental data and the original model of the HS-Eden machine.

Feature of interest	Experimental data	Original model	Absolute error	Error %
NX(1,1) first resonance frequency	665.35 Hz	830.39 Hz	165.04 Hz	24.81
NX(1,1) first anti-resonance frequency	687.43 Hz	815.5 Hz	128.06 Hz	18.63
DX(3,3) first resonance frequency	671.21 Hz	830.39 Hz	159.18 Hz	23.72
DX(3,3) first anti-resonance frequency	601.97 Hz	740.63 Hz	138.67 Hz	23.04
NX(1,1) first resonance damping ratio	0.011051	0.0020003	0.0090511	81.90
NX(1,1) first anti-resonance damping ratio	0.0056576	0.0019593	0.0036983	65.37
DX(3,3) first resonance damping ratio	0.010003	0.0020003	0.008003	80.00
DX(3,3) first anti-resonance damping ratio	0.010253	0.0017652	0.0084873	82.78

Significant difference can be seen between experimental data and the original model from Table 6.4. This can also be seen on the NX and DX-axes bode plots which are shown in Figure

6.6. Also bode plots related to the coupling between NX- and DX-axes are shown. In this coupled case, excitation input and output is located on a different axis. When excitation input is located at NX-axis, output is located at DX-axis and vice versa.

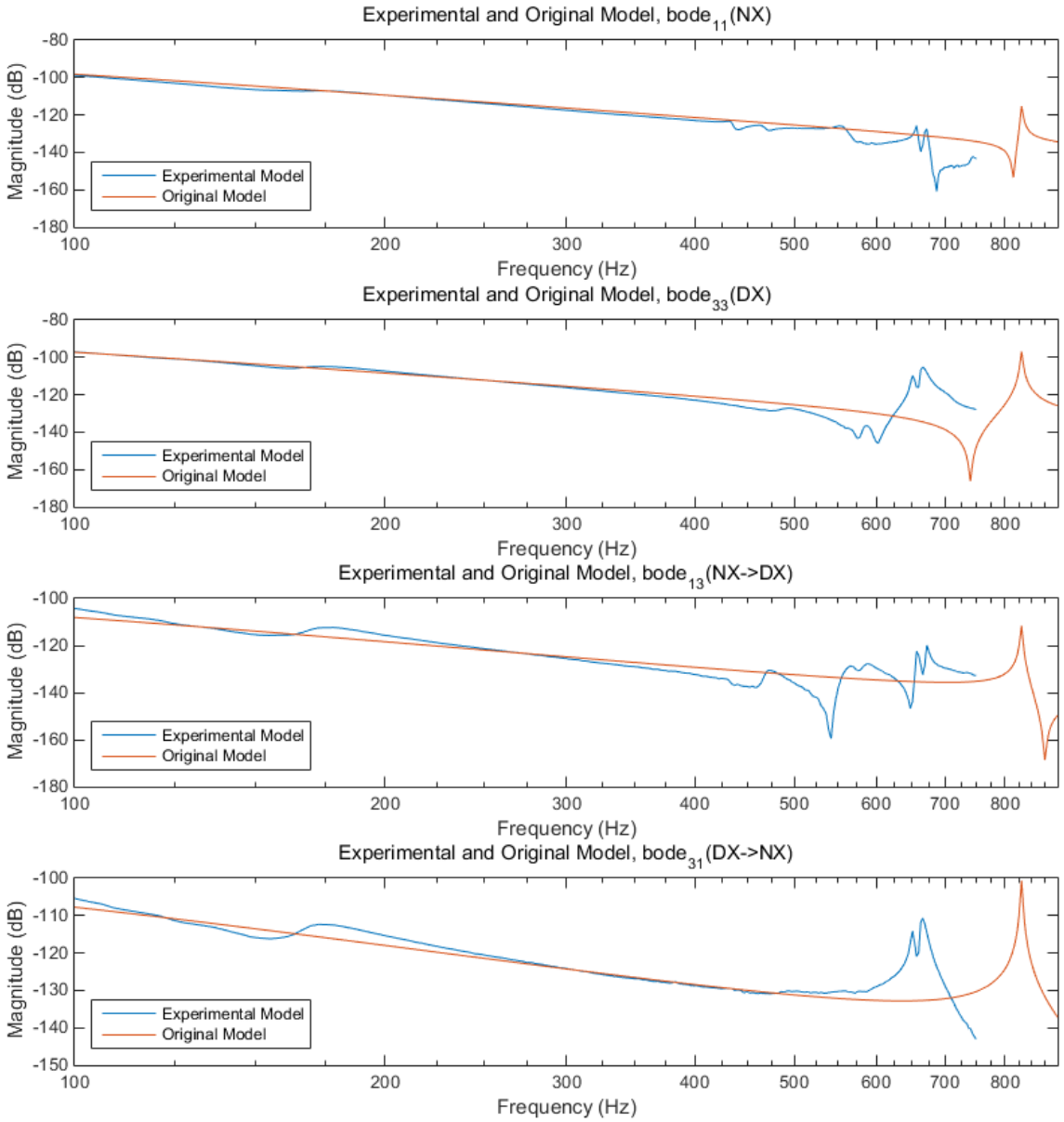

Fig. 6.6. Bode plots from the NX- and DX-axes and coupled case between experimental and the original model of the HS-Eden machine.

After randomizing the starting values of design variable vector ***e***, rotor model of the HS-Eden machine was updated. Weights for resonance frequency $w_{\mathrm{f},k}^{\mathrm{r}}$, anti-resonance frequency $w_{\mathrm{f},k}^{\mathrm{a}}$, resonance frequency damping ratio $w_{\mathrm{d},k}^{\mathrm{r}}$ and anti-resonance frequency damping ratio $w_{\mathrm{d},k}^{\mathrm{a}}$ were assumed to be 1. Weight w_{d} used to decrease the effect of total damping ratio error in the total error was 0.01. In Table 6.5 comparison of the experimental and the updated model is shown.

Table 6.5. Comparison of the experimental data and the updated model of the HS-Eden machine.

Feature of interest	Experimental data	Updated model	Absolute error	Error %
NX(1,1) first resonance frequency	665.35 Hz	671.21 Hz	5.8577 Hz	0.8804
NX(1,1) first anti-resonance frequency	687.43 Hz	687.43 Hz	≈ 0 Hz	≈ 0
DX(3,3) first resonance frequency	671.21 Hz	671.21 Hz	≈ 0 Hz	≈ 0
DX(3,3) first anti-resonance frequency	601.97 Hz	600.94 Hz	1.024 Hz	0.1701
NX(1,1) first resonance damping ratio	0.011051	0.0020006	0.0090508	81.90
NX(1,1) first anti-resonance damping ratio	0.0056576	0.0020664	0.0035911	63.48
DX(3,3) first resonance damping ratio	0.010003	0.0020006	0.0080027	80.00
DX(3,3) first anti-resonance damping ratio	0.010253	0.0017854	0.0084671	82.59

Bode plot between NX- and DX-axes of the experimental data and updated model are shown in Figure 6.7. In this case also the coupling case bode plots are shown.

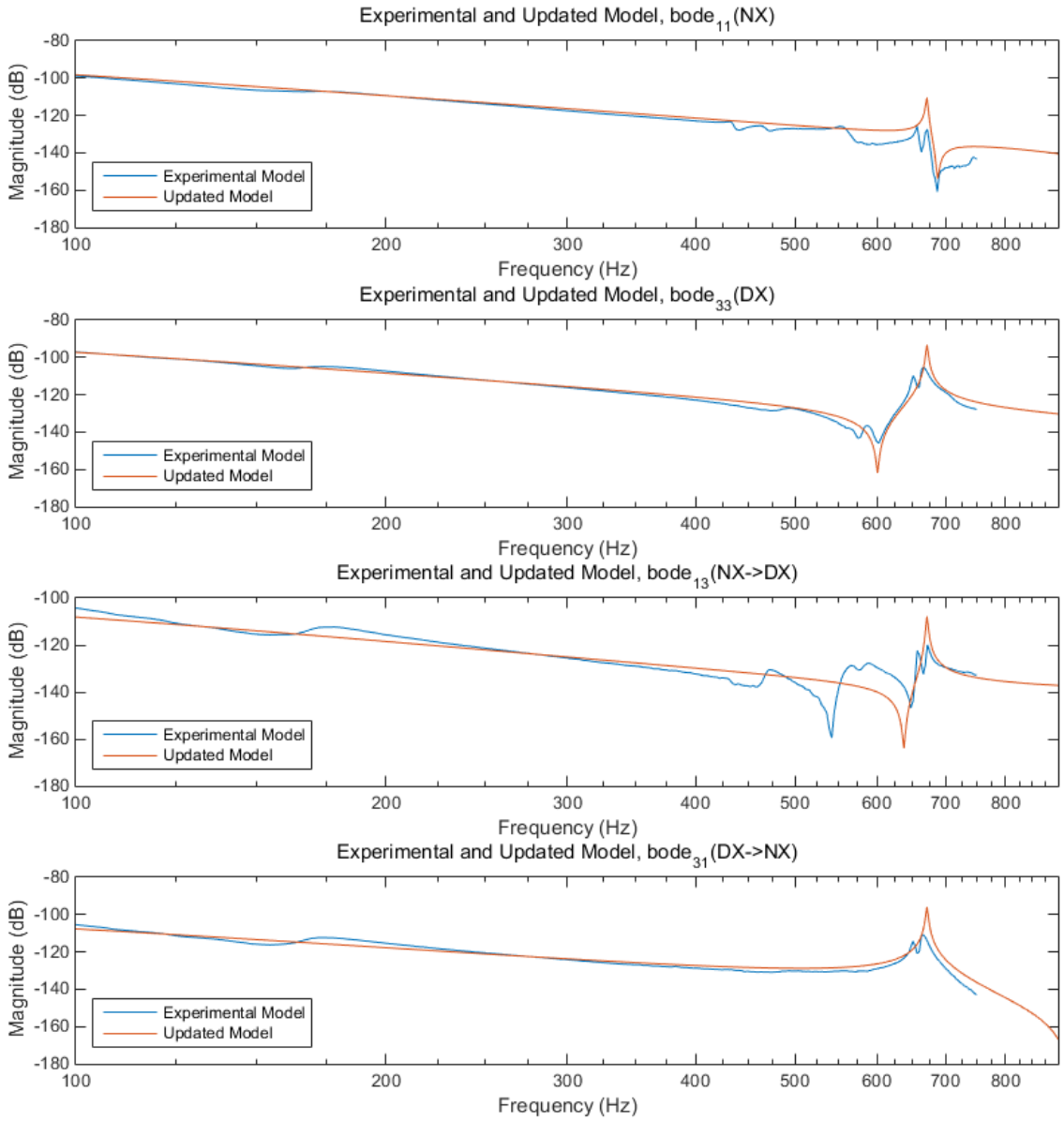

Fig. 6.7. Bode plots from the NX- and DX-axes and coupled case between experimental and the updated model of the HS-Eden machine.

From Table 6.5 and Figure 6.7 it can be seen that the resonance and anti-resonance frequency error between experimental data and model has decreased. Largest frequency error is now less

than 1.0 %. For the damping ratios error remained almost the same between comparison of experimental data with original and updated model. One cause of this is the selected weights and also the parametric model generation seems to fit the frequency better than the damping ratio. Figure 6.8 shows the updated elasticity values e_p from updated model.

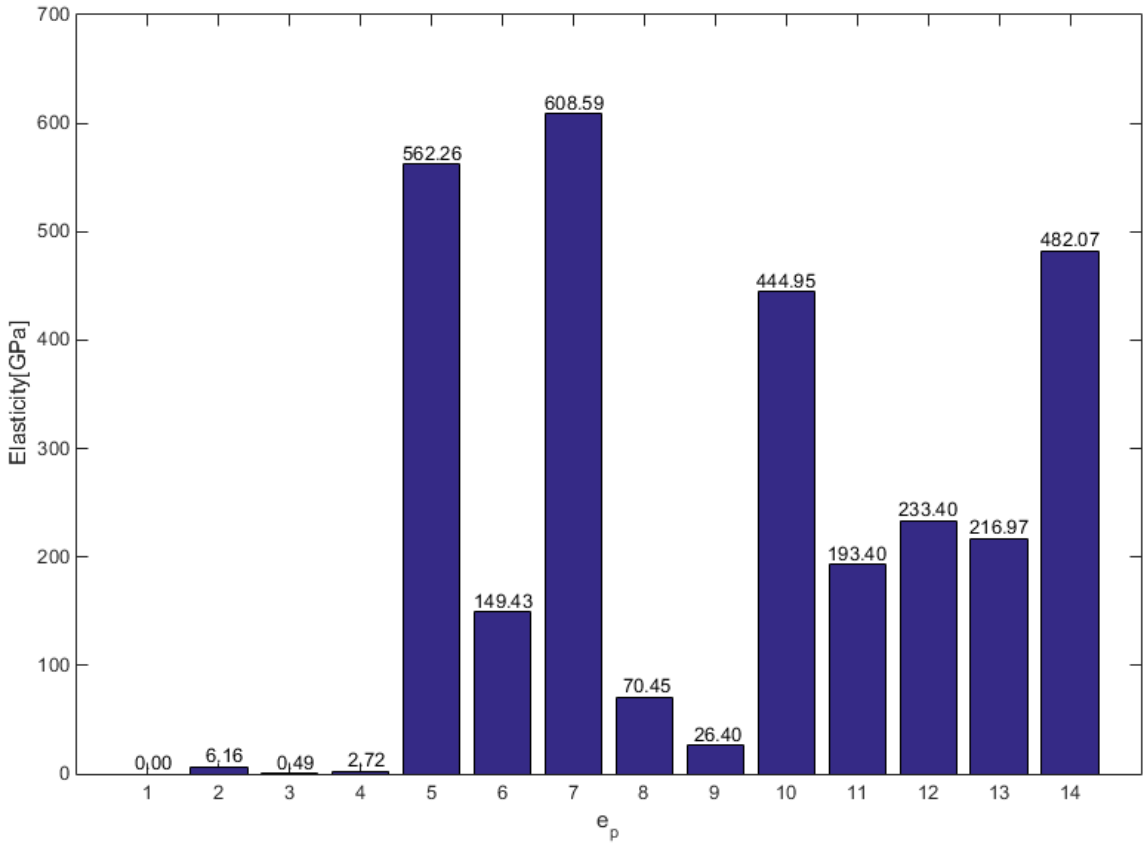

Fig. 6.8. Elasticity values e_p from the updated HS-Eden model. Elasticity value of e_1 is 0.18 MPa. Nominal elasticity value of the elements was 200 GPa.

From Figure 6.8 it can be seen that the elasticity values of the outer part of the first radial AMB (1…4) is almost zero and the outer part of the second radial AMB (5…8) has quite big values. Reason for this might be the different press force applied to the first and second radial AMB lamination stack.

Figure 6.9 shows the output of the function $B(\boldsymbol{e})$(error function) for each iteration step of the Nelder-Mead optimization method during the HS-Eden rotor model update. In this case there are 1000 iteration steps.

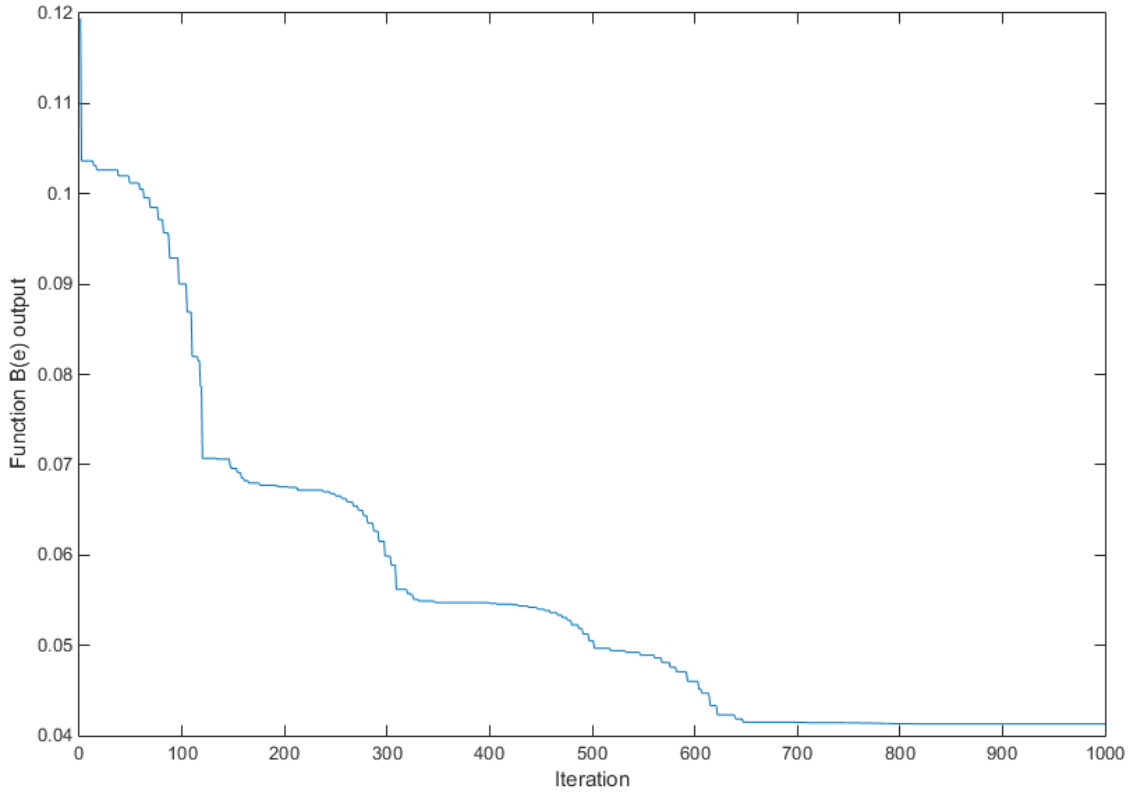

Fig. 6.9. Output of the function $B(\boldsymbol{e})$ during the HS-Eden rotor model update.

From Figure 6.9 it can be noted, that the optimization of the rotor model starts to converge rapidly during the first 120 iterations and the output of the function $B(\boldsymbol{e})$ is almost halved compared to the starting output. Optimization in this case could be stopped at around 650 iterations, because output of the function $B(\boldsymbol{e})$ stays almost constant during the later iteration steps.

In conclusion an updated model was obtained for the HS-Eden machine. Rotor model update procedure with 14 design variables e_p ran at about 11.55 iterations per second.

7 CONCLUSIONS

Main point of the thesis was to focus on the magnetic center calibration, rotor model identification and rotor model updating method design, implementation and testing. All mentioned methods were tested with the HS-Eden machine. In the design of these methods, the ability to use different machines with ease was taken into account. Research problem of the thesis “finding ways to reduce the uncertainty related to the model based control” was solved with these methods.

With the magnetic center calibration, magnetic center of the rotor is located. An algorithm using several bias current values was developed. This magnetic center is an optimal operating point of the AMB system, because in this point the system corresponds better to the linearized equations. Magnetic center of the HS-Eden machine is located approximately at (70.7, 10.49, 148.66, -20.65) µm from the geometric center.

Identification of the rotor is used to obtain the frequency response of the rotor-bearing system. An adaptive amplitude stepped-sine identification algorithm was developed. The identified rotor model could be used to locate flexible modes of the rotor. First flexible mode of all the radial axes (DX, DY, NX, NY) of the HS-Eden machine is located at between 600…700 Hz.

Rotor model update is a method used to obtain a model which describes more accurately the experimental data of the rotor model identification. A method for constructing parametric model of the rotor from experimental data used to extract resonance and anti-resonance frequencies and damping ratios was presented. This method was then used in the rotor model updating method which was developed. With the rotor model update method, a more accurate model was obtained for the HS-Eden machine. Largest frequency error between experimental data and the updated model was less than 1.0 %. For the damping ratios error between experimental data and original and updated model remained almost the same.

Future work with the magnetic center calibration would include the testing of optimal number of bias currents and the optimal bias current values. Measurement data could be saved to a file. Axial magnetic center calibration also could be considered.

For the rotor model identification, multi-sine excitation with the Beckhoff PLC system could be developed. Also better frequency range selection is needed. For the Z-axis identification even a different frequency vector. Excitation at the controller input $\boldsymbol{E}$ so that for example controller performance could be measured.

For the rotor model updating, future work would include testing of other optimization methods. Finding good starting values for the design variables e_p is needed. Also testing and including other flexible modes in the error calculation. FEM-model generation should be checked and optimized if possible. Parametric model generation and damping ratio extraction should be checked.

REFERENCES

Beckhoff (2012) Beckhoff flyer about TwinCAT, available at

http://download.beckhoff.com/download/document/catalog/Beckhoff_TwinCAT3_042012_e.pdf accessed 2.10.2015

Gähler, C. & Förch, P. (1994a) A precise magnetic exciter for rotordynamic experiments, Fourth International Symposium on Magnetic Bearings, ETH Zürich, Switzerland

Gähler, C. & Herzog, R. (1994b) Identification of Magnetic Bearing Systems, Fourth International Symposium on Magnetic Bearings, ETH Zürich, Switzerland

Gähler, C. (1998) Rotor Dynamic Testing and Control with Active Magnetic Bearings, Doctoral thesis, ETH Zürich, Switzerland

Gibbs P. & Geim, A. (1997) Physics FAQ about levitation,

http://math.ucr.edu/home/baez/physics/General/Levitation/levitation.html accessed 9.11.2015

Hynynen, K. M. & Jastrzebski, R. P. & Smirnov, A. (2010) Experimental Analysis of Frequency Response Function Estimation Methods for Active Magnetic Bearing Rotor System, The Twelfth International Symposium on Magnetic Bearings (ISMB 12), Wuhan, China

Hynynen, K. (2011) Broadband excitation in the system identification of active magnetic bearing rotor systems, Doctoral Thesis, Lappeenranta University of Technology, Finland

ISO 14839-3 (2006) Mechanical vibration - Vibration of rotating machinery equipped with active magnetic bearings - Part 3: Evaluation of stability margin. International Organization for Standardization ISO

Jastrzebski, R. P. & Hynynen, K. M. & Smirnov, A. & Pyrhönen, O. (2012) Influence of the drive and dc link generated disturbances on an AMB control system, Electr. Rev., vol. 2012, no. 1a, pp. 247–253

Keesman, J. K. (2011) System Identification An Introduction, Springer.

Levy, E. C. (1959) Complex-Curve Fitting, Ire Transactions on Automatic Control, Vol AC-4 pp. 37-44

Ljung, L. (1987) System Identification Theory for the User, Prentice-Hall, Englewood Cliffs, New Jersey

Lösch, F. (2002) Identification and Automatic Controller Design for Active Magnetic Bearing Systems, Doctoral Thesis ETH Zürich, Switzerland

Marshall, J. T. (2001) A Multi-Point Measurement Technique for the Enhancement of Force Measurement with Active Magnetic Bearings (AMB), Master's thesis, Virginia Polytechnic Institute and State University, Blacksburg, Virginia

Nelder, J. A. & Mead, R. (1965) A simplex method for function minimization, The Computer Journal 7(4) pp.308-313

Prins, R. J. & Kasarda, M. E. F & Prins, S. C. B (2007) A System Identification Technique Using Bias Current Perturbation for Determining the Effective Rotor Origin of Active Magnetic Bearings, Journal of Vibration and Acoustics, Vol.129 pp. 317-322

Schweitzer, G. & Maslen, E. H. (eds.) (2009) Magnetic Bearings, Theory, Design, and Application to Rotating Machinery, Springer

Smirnov, A. (2012) AMB System for high-speed rotors using automatic commissioning, Doctoral Thesis, Lappeenranta University of Technology, Finland

Smirnov, A. (2015) Magnetic bearings for the PoC, internal design report, Lappeenranta University of Technology, Finland

Verboven, P. (2002) Frequency-domain system identification for modal analysis, Doctoral thesis, Vrije Universitet Brussel, Belgium

Wróblewski, A. C. (2011) Model identification, updating, and validation of an active magnetic bearing high-speed machining spindle for precision machining operation, Doctoral thesis, Cleveland state university, Cleveland, Ohio

APPENDICES

Appendix 1: Rotor model update MATLAB® script

```
clear all
close all
clc
format shortG
set(cstprefs.tbxprefs,'FrequencyUnits','Hz')
run('Data_05_06_2015_15_03_49.m'); %load identification data
%FRFs from identification data
sys_plantdx =
idfrd(data_exc_dx(:,7)./data_exc_dx(:,3)/1e6,2*pi*data_exc_dx(:,1),50e-6);
sys_plantnx =
idfrd(data_exc_nx(:,9)./data_exc_nx(:,5)/1e6,2*pi*data_exc_nx(:,1),50e-6);
addpath(strcat(pwd,'\AMBLib'));
freq_p_in=[];
freq_z_in=[];
damp_p_in=[];
damp_z_in=[];
%determining resonance and anti-resonance frequencies and damping ratios
%from experimental data using least squares optimization
[freq_p,freq_z,damp_p,damp_z]=pz_from_exp(sys_plantnx);
freq_p_in(end+1)=freq_p(6);
freq_z_in(end+1)=freq_z(5);
damp_p_in(end+1)=damp_p(6);
damp_z_in(end+1)=damp_z(5);
[freq_p,freq_z,damp_p,damp_z]=pz_from_exp(sys_plantdx);
freq_p_in(end+1)=freq_p(6);
freq_z_in(end+1)=freq_z(3);
damp_p_in(end+1)=damp_p(6);
damp_z_in(end+1)=damp_z(3);
n_design=14;
var_low=0;
var_up=2;
E_design=ones(1,n_design)*200e9;
n_res=1;
n_antires=1;
opt_fmin=optimset('MaxIter',1000,'MaxFunEvals',2500);
x_start=((var_up-var_low)*rand(1,n_design)+var_low).*E_design; %initial
quess e
[x1,fval,exitflag,output]=fminsearch(@(x)
operator_be(x,n_res,n_antires,freq_p_in,freq_z_in,damp_p_in,damp_z_in),x_st
art,opt_fmin) %Nelder-Mead optimization, operator_be is the error function
B(e)
%after Nelder-Mead optimization has finished, x1 contains the updated
%elasticity values e_p
```